High Strain Rate Elasto-Plasticity Identification using the Image-Based Inertial Impact (IBII) Test Part 1: Error Quantification

Lloyd Fletcher[1] Frances Davis[1] Sarah Dreuilhe[1] Aleksander Marek[1]
Fabrice Pierron[1]
[1]Mechanical Engineering, Faculty of Engineering and Physical Sciences,
University of Southampton, UK

Abstract

Current high strain rate testing procedures generally rely on the split Hopkinson bar (SHB). In order to gain accurate material data with this technique it is necessary to assume the test sample is in a state of quasi-static equilibrium so that inertial effects can be neglected. During the early portion of an SHB test it is difficult to satisfy this assumption making it challenging to investigate the elastic-plastic transition for metals. With the development of ultra-high speed imaging technology the image-based inertial impact (IBII) test has emerged as an alternative to the SHB. This technique uses full-field measurements coupled with the virtual fields method to identify material properties without requiring the assumption of quasi-static equilibrium.

The purpose of this work is to develop the IBII method for the identification of elasto-plasticity in metals. In this paper (part 1) the focus is on using synthetic image deformation simulations to analyse identification errors for two plasticity models, a simple linear hardening model and a modified Voce model. Additionally, two types of virtual fields are investigated, a simple rigid body virtual field and the recently developed sensitivity-based virtual fields. The results of these simulations are then used to select optimal processing parameters for the experimental data analysed in part 2.

1 Introduction

The behaviour and failure mechanisms of metals are often dependent on strain rate. These differences are critical when designing structures or components that are subjected to impact or blast loads. To accurately design for impact loads, the elasto-plastic response of metals under high strain rate loading must be accurately characterised.

Numerous methods for characterising the high strain rate response of metals have been proposed [1]; however, the split-Hopkinson bar (SHB) has been by far the most popular method to study material behaviour at strain rates on the order of $10^3\ s^{-1}$. Analysis of standard SHB data relies on one-dimensional wave propagation theory to calculate the stress, strain, and strain rate in the specimen during the test. It is also necessary to assume that the stress and strain state in the sample is uni-axial and uniform. As a result, there are some inherent limitations with the data gathered from SHB tests.

One of the primary issues that corrupt the stress-strain data from the SHB test is inertial effects [2]. Inertial effects invalidate measurements at the start of the test making it impossible to characterise the mechanical response at high strain rates and low strains. As a result, it is impossible to determine the elastic modulus of materials that yield or damage at low strains. This also impacts the ability of the SHB technique to accurately describe the transition between elasticity and plasticity for metals. Additionally, the requirement that the sample must undergo uni-axial deformation and one dimensional wave propagation strongly limits the stress-states which can be tested with the traditional SHB technique. This makes it difficult to fully characterise the yield surface at high strain rates for the case of anisotropic plasticity. Given the limitations of SHB tests alternative methods of characterising the high strain response of metals must be explored. The recent developements in ultra-high speed imaging [3, 4] and full-field measurement techniques provide a unique opportunity to improve the quality of high strain rate test data.

The development of modern ultra-high speed cameras has made recording the full-field deformation of solids possible at rates up to 5 $Mfps$ with unprecedented image quality. The surface of the specimen can be imaged and, as a result, data processing no longer needs to rely on point based measurements from strain gauges. Digital image correlation (DIC) [5] and the grid method [6] are techniques that can extract full-field displacement measurements from images. These full-field measurement techniques are now employed alongside traditional SHB measurements to calculate the strain distribution in the specimen [7, 8]. More recently, researchers have begun to use inverse methods, such as finite element updating [9–11] and the virtual fields method [12,13], to identify material parameters from full-field data collected during high strain rates tests. From this a whole new class of inertial test methods have evolved. In this case it is not necessary to assume the sample is in a state of quasi-static equilibrium as the acceleration fields are measured and used as the force measurement. This has included the use of full or partial inertial loading to identify the dynamic material parameters for concrete [13–15], composites [16], polymeric foams [17, 18] and rubbers [19–21].

A more recently developed methodology is the image-based inertial impact (IBII) test. Thus far the use of the IBII methodology has focused on the linear elastic properties of brittle and quasi-brittle materials such as composites [22–24] and cermets [25]. However, there is considerable scope to use the IBII method for identifying non-linear material models. A first attempt at this was made in [26, 27] to identify the rate sensitivity parameter of a Johnson-Cook model using the IBII test on titanium. However, the identification of the hardening law parameters was not considered. Therefore, the present work focuses on the identification of hardening law parameters using the IBII test with a specific objective of investigating the transition between elasticity and plasticity where the traditional SHB technique has difficulty.

The overall aim of the current work is to design and validate an experimental technique to identify non-linear elasto-plastic material models using the IBII method. Two materials will be used in this work: 1) aluminium 6082-T6, as its plastic response exhibits no rate sensitivity [28–31] and thus comparison with quasi-static data for this material serves as a baseline; and 2) stainless steel 316L which shows some sensitivity to strain rate [32–34]. This work is divided into two parts. The first part is purely computational, focusing on the development and validation of the required VFM theory as well as processing parameter selection and error quantification using synthetic image deformation simulations. The second part presents an experimental validation of the method. This paper (part 1) begins by describing the VFM theory for elasto-plastic identification in Section 2. The next section describes a finite element model of the IBII configuration and uses kinematic data from this model to validate the VFM identification procedure (Section 3). The final major section of this paper uses image deformation simulations (see for example [23, 25, 26, 35–38]) to simulate the impact of the errors arising from the experimental measurement system on the identified material parameters. The results of these simulations are used to select the near optimal smoothing parameters for the experimental data and to estimate the systematic and random errors of the experimental identification.

2 The Virtual Fields Method

The virtual fields method is an inverse technique that uses the principle of virtual work combined with full-field measurements to identify material properties. The principle of virtual work is given by:

$$\overbrace{\int_S \boldsymbol{T}\cdot\boldsymbol{u^*}\,\mathrm{d}S + \int_V \boldsymbol{b}\cdot\boldsymbol{u^*}\,\mathrm{d}V}^{W^*_{ext}} - \overbrace{\int_V \boldsymbol{\sigma}:\boldsymbol{\varepsilon}^*\,\mathrm{d}V}^{W^*_{int}} = \overbrace{\int_V \rho\,\boldsymbol{a}\cdot\boldsymbol{u^*}\,\mathrm{d}V}^{W^*_{acc}} \tag{1}$$

where $\boldsymbol{T}$ is the traction vector, $\boldsymbol{b}$ is the body force vector, $\boldsymbol{\sigma}$ is the stress tensor, and $\boldsymbol{u^*}$ and $\boldsymbol{\varepsilon}^*$ are the virtual displacement vector and associated virtual strain tensor, respectively. The term on the right hand side of the equation is the virtual work due to acceleration where $\boldsymbol{a}$ is the acceleration vector and ρ is the density of the material. The dot (or scalar) product between vectors is denoted '$\cdot$' and the double dot product between second order tensors is denoted '$:$'. Equation 1 expresses the global equilibrium between the virtual work of internal stresses, W^*_{int}, the virtual work of external forces, W^*_{ext}, and the virtual work due to acceleration, W^*_{acc}. In this expression, the virtual displacement, $\boldsymbol{u^*}$, does not have any physical meaning, and can be any test function which is continuous and piecewise differentiable over the whole volume. The virtual strains are derived from virtual displacements as: $\varepsilon^*_{ij} = \frac{1}{2}\left(\frac{\partial u^*_i}{\partial j} + \frac{\partial u^*_j}{\partial i}\right)$.

Let us consider applying equation 1 to the IBII test configuration shown in Figure 1. For a dynamically loaded IBII specimen, the acceleration can be derived from the measured displacement field by double temporal differentiation. Note that the body force term generally only contains gravity and is negligible for the IBII test configuration considered here. The kinematic fields in equation 1 are all functions of space and time. Here the function notation has been omitted for simplicity.

Most full-field measurement techniques only provide information at the surface of the solid, therefore some assumption on the behaviour through the thickness must be made to calculate the volume integrals in equation 1. For the IBII test, the assumption of plane stress with uniform kinematic fields through-thickness is used since the specimens under consideration are thin and only loaded in plane using an edge-on impact configuration. Using these assumptions and neglecting the influence of body forces, equation 1 can be rewritten as:

$$\overbrace{\int_S \boldsymbol{\sigma}:\boldsymbol{\varepsilon}^*\mathrm{d}S}^{W^*_{int}} - \overbrace{\int_l \boldsymbol{T}\cdot\boldsymbol{u}^*\mathrm{d}l}^{W^*_{ext}} + \overbrace{\int_S \rho\,\boldsymbol{a}\cdot\boldsymbol{u}^*\mathrm{d}S}^{W^*_{acc}} = 0 \tag{2}$$

where S indicates the two dimensional surface of the specimen and l indicates the perimeter. A constitutive relationship, $\boldsymbol{\sigma} = \boldsymbol{\sigma}(\boldsymbol{\varepsilon}, \mathbf{K})$, which relates the measured strains and unknown constitutive parameters, $\mathbf{K}$, to the stress is needed to calculate the first term in equation 2. For a linear elastic material, equation 2 produces a set of linear equations that can be solved to identify the constitutive parameters. However, when a non-linear constitutive relationship is used, equation 2 produces a set of non-linear equations. For the case of elasto-plasticity, there is no explicit relationship between the measured strain and the stress and therefore the stress components can only be calculated using an iterative stress reconstruction algorithm which separates the strain into its elastic and plastic contributions. To solve the set of non-linear equations, a cost function representing the sum of the internal, external, and inertial virtual work is constructed:

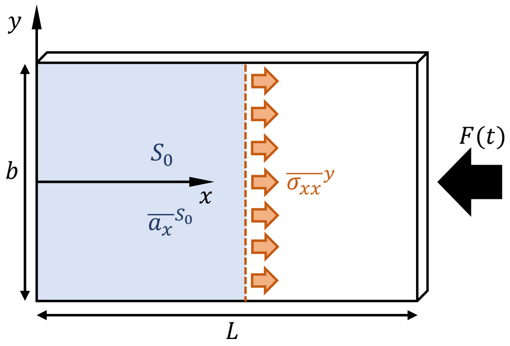

Figure 1: Thin rectangular IBII specimen loaded edge-on by a time varying impact force $F(t)$. The average stress over any vertical cross-section at x (the dashed line) can be found using equation 4.

$$C_f(\mathbf{K}) = \sum_{t=t_0}^{t_f} \left(\int_S \boldsymbol{\sigma}\left(\boldsymbol{\varepsilon}, \mathbf{K}\right) : \boldsymbol{\varepsilon}^* \, \mathrm{d}S - \int_l \boldsymbol{T} \cdot \boldsymbol{u}^* \mathrm{d}l + \int_S \rho \, \boldsymbol{a} \cdot \boldsymbol{u}^* \, \mathrm{d}S \right)^2 . \tag{3}$$

where the summation is performed over a given set of time steps t from the first frame considered at t_0 to the final frame t_f. The cost function is minimised by updating the constitutive model parameters, noting that for each iteration the stress reconstruction must be performed to calculate the internal virtual work.

2.1 Selection of the Virtual Fields

The virtual displacement, $\boldsymbol{u}^*$, in equation 2 can be chosen to derive as many equations as necessary to identify the material parameters. Two types of virtual fields will be considered here, a simple rigid body virtual field (*i.e.* the stress-gauge virtual field) and sensitivity-based virtual fields.

Stress-gauge (SG) virtual field: consider the schematic of an IBII sample as shown in Figure 1. Here we apply a virtual field describing a rigid translation along the 'x' axis as follows: $u_x^* = 1$, $u_y^* = 0$ and $\epsilon_{xx}^* = \epsilon_{yy}^* = \epsilon_{xy}^* = 0$. This virtual field cancels out the contribution of internal virtual work, W_{int}^*, leaving only the external virtual work, W_{ext}^*, and inertial virtual work, W_{acc}^*. Substituting this rigid body virtual field into equation 2 and approximating the integrals as discrete sums as in [16, 22, 23, 25] gives:

$$\overline{\sigma_{xx}}^{y} = \rho x \overline{a_x}^{S_0} \tag{4}$$

where $\overline{\sigma_{xx}}^{y}$ is the average stress over the axial section at the position x. Here the overline notation is used to indicate spatial averaging with a superscript 'y' indicating the average over an axial slice whereas a superscript S_0 indicates averaging from the free edge to the axial section of interest at x. Thus, $\overline{a_x}^{S_0}$ is the average acceleration over the surface from the free-edge to the axial section of interest. Note that these spatial averages are shown schematically in Figure 1. Equation 4 is referred to as the 'stress-gauge' because the virtual work of acceleration, W_{acc}^*, acts like a load cell allowing the average stress in any vertical section of the specimen to be calculated from the density and surface average of the acceleration.

Sensitivity-based (SB) virtual fields: sensitivity-based virtual fields were developed as a method to automatically generate virtual fields for non-linear problems [39]. This approach uses stress sensitivity maps to perturb each model parameter, defined as:

$$\delta\boldsymbol{\sigma}^{(i)}\left(\boldsymbol{\varepsilon}, \boldsymbol{K}, t\right) = \boldsymbol{\sigma}\left(\boldsymbol{\varepsilon}, \boldsymbol{K}, t\right) - \boldsymbol{\sigma}\left(\boldsymbol{\varepsilon}, \boldsymbol{K} + \delta K_i, t\right) \tag{5}$$

where $\boldsymbol{K}$ is the vector of model parameters, i denotes the i^{th} model parameter in vector $\boldsymbol{K}$, δK_i is a small perturbation to the model parameter K_i, and t is the time step. The stress sensitivity maps naturally identify the regions where relevant information is encoded for identifying each parameter. In regions where $\delta\boldsymbol{\sigma}^{(i)}$ is close to zero the change in stress due the perturbation is small while large values of $\delta\boldsymbol{\sigma}^{(i)}$ indicate that small changes in K_i significantly impact the stress. Maps of the stress sensitivity are produced for each model parameter and these maps show the regions in space which are sensitive to each model parameter. These stress sensitivity maps are calculated at each time step of the test and are used to produce the virtual displacements using a virtual mesh so that the virtual strain spatial distribution resembles that of the stress sensitivity for each parameter. Each model parameter in $\boldsymbol{K}$ has its own stress sensitivity map resulting in a virtual field which ‘highlights’ areas where the parameter is activated. In this work the total stress sensitivity is used as described in [39]. Full details on the implementation of these sensitivity-based virtual fields can be found in Marek et al. [39].

2.2 Plasticity Models

The initial analysis will focus on the identification of a simple linear hardening rule to demonstrate and validate the VFM theory described previously. As there are only two parameters to identify (*i.e.* yield stress and hardening modulus) it is relatively simple to visualise. For all cases considered here a von Mises yield criterion is used. For a linear hardening model the updated yield stress σ_y is given by:

$$\sigma_y = \sigma_0 + H\epsilon_p \tag{6}$$

where σ_0 is the initial yield stress, H is the hardening modulus and ϵ_p is the equivalent plastic strain. In the later sections of this article the linear hardening law is denoted using the shorthand ‘LH’. In practice, more complex hardening laws more accurately represent the elasto-plastic behaviour of metals. Here the focus is on the transition between elastic and plastic behaviour so a modified Voce model is also considered:

$$\sigma_y = \sigma_0 + R_{inf}(1 - exp(-b\epsilon_p)) + R_0\epsilon_p \tag{7}$$

where σ_0 is the initial yield stress and R_0 is the long term hardening modulus. The additional parameters R_{inf} and b describe the non-linear transition region from the initial yield stress to the long term hardening modulus. For this plasticity model there is considerable interaction between the σ_0 and R_{inf} parameters with different combinations of these parameters returning similar solutions. Here we define the effective initial yield stress as $\sigma_{YS} = \sigma_0 + R_{inf}$ which is similar to the initial yield stress given for the linear hardening model. The Voce hardening law is denoted with the use of the shorthand ‘VH’ in subsequent sections of this article.

2.3 Inverse Parameter Identification

Stress-gauge virtual field (SG): using equation 3 the following cost function is found for the stress-gauge virtual field (equation 4):

$$C_f^{SG}(\mathbf{K}) = \sum_{x=x_0}^{x_n} \sum_{t=t_0}^{t_f} \left(\overline{\sigma_{xx} \left(\mathbf{K}, \boldsymbol{\varepsilon} \right)}^{y} - \rho x \overline{a_x}^{S_0} \right)^2 \tag{8}$$

where the summation is considered over a given number of time steps (t) as for equation 3 and a given number of axial sections (x) between the first section considered from the free edge x_0 and the furthest section from the free edge x_n. This cost function is effectively the squared difference between the average axial stress reconstructed using the constitutive equation and that reconstructed from the acceleration. Note that there is no requirement to include all time steps or all axial sections in the cost function. In subsequent sections of this article identifications performed with the stress-gauge virtual field are denoted by using the shorthand 'SG'. This designation allows identifications performed with the SG virtual field to be differentiated from the sensitivity-based virtual fields which are described next.

Sensitivity-based virtual fields (SB): the following cost function is used for identifications performed with the sensitivity-based virtual fields:

$$C_f^{SB}(\mathbf{K}) = \sum_{i=1}^{n} \frac{1}{\left(\alpha^{(i)}\right)^2} \left[\sum_{t=t_0}^{t_f} \left(\overline{\boldsymbol{\sigma} \left(\varepsilon, \boldsymbol{K} \right) : \boldsymbol{\varepsilon}^{*(i)}}^{S} - \rho \, \overline{\boldsymbol{a} \cdot \boldsymbol{u}^{*}}^{S} \right)^2 \right] . \tag{9}$$

where n is the number of model parameters in $\boldsymbol{K}$ and $\alpha^{(i)}$ is a weight parameter to ensure that each parameter has approximately the same contribution to the cost function. The weight, $\alpha^{(i)}$, is the mean of the m highest internal virtual work W_{int}^{*} values. In this case the overline notation coupled with a superscript 'S' is used to indicate a spatial average over the whole surface of the sample. Note that equation 9 was derived assuming that the virtual field were specified to eliminate the contribution of the impact force to the external virtual work term. This is easily achieved by enforcing $\boldsymbol{u}^{*} = 0$ over the impacted edge. The surface over which the cost function is evaluated can be further restricted by applying virtual boundary conditions that eliminate the contribution of unknown forces on all boundaries of the sample. As with equation 8 it is not necessary to include all time steps. The most notable difference between the cost functions is that equation 8 only involves σ_{xx} and a_x while equation 9 includes contributions from the entire stress tensor and both acceleration components. The ability of both types of virtual fields to identify the constitutive parameters is validated using finite element data in the following section (Section 3). Identifications performed with the sensitivity-based virtual fields are given the abbreviation 'SB' for the remainder of this article.

3 Numerical Validation

3.1 Finite Element Model

An explicit dynamics finite element model of the IBII test configuration was constructed in Abaqus Explicit v6.14. A schematic of the model is shown in Figure 2. The model was constructed in 2D using the plane stress assumption with CPS4R elements (4-node, reduced integration). The time step was allowed to float using the default setting in Abaqus, where it is set to 0.8 t_{crit} with t_{crit} given by the minimum time taken for a longitudinal wave to traverse an element in the simulation. All components in the simulation were modelled as isotropic elasto-plastic using a von Mises yield criterion. The specimen was modelled using the material properties of aluminium 6082-T6 or stainless steel 316L to replicate the two materials considered in the experiments. Preliminary quasi-static experiments were used to obtain the elastic

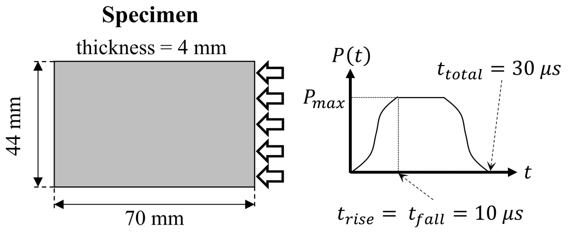

Figure 2: Schematic of the finite element model showing the geometry and temporal evolution of the applied pressure pulse.

Elastic Properties	Aluminium (Al) 6082-T6	Steel (St) 316L
$\rho\ [kg.m^{-3}]$	2700	7850
$E\ [GPa]$	70	190
$\nu\ [-]$	0.33	0.29
Linear Hardening (LH)	Aluminium	Steel
$\sigma_0\ [MPa]$	280	425
$H\ [MPa]$	1800	5000
Voce Hardening (VH)	Aluminium	Steel
$\sigma_0\ [MPa]$	190	300
$R_0\ [MPa]$	1800	5000
$R_{inf}\ [MPa]$	90	125
$b\ [-]$	2000	1000

Table 1: Density and elasto-plastic material properties for the finite element models.

(Table 1) and representative plastic material parameters (Table 1) used in the simulations. Note that for the 316L steel the properties are expected to be rate sensitive so analysis of literature data [32, 33] and preliminary processing of the IBII experimental data was used to estimate the high rate properties.

In order to input the Voce hardening law into Abaqus it is necessary to provide a table of yield stress and equivalent plastic strain values. This was achieved using a Python script that discretised the plastic response into 1 $\mu\epsilon$ increments between 0 and 20% equivalent plastic strain. To replicate the loading observed in a typical IBII test a pressure pulse was applied to one ‘short’ edge of the rectangle and the remaining edges were free. The temporal evolution of this pulse was approximately trapezoidal with the temporal shape of the rising and falling edge being specified using the ‘smooth step’ option in Abaqus. The ‘smooth step’ option defines the ramp as a smoothly varying cubic function over the specified time frame. A rise/fall time of $t_{rise} = t_{fall} = 10\ \mu s$ and a total duration of $t_{total} = 30\ \mu s$ was used based on analysis of experimental data. The peak pressure of the pulse was $P_{max} = 360\ MPa$ for the aluminium model and $P_{max} = 658\ MPa$ for the steel model base on the results of preliminary experiments. Kinematic data (displacement, acceleration, stress and strain fields) were extracted from the specimen at intervals of 0.2 μs to replicate the frame rate of the camera used for the experiments (*i.e.* 5 MHz). Note that the Python code used to create the Abaqus FE model for each case is given in the digital dataset described at the end of the article.

The purpose of the finite element models was to validate the identification procedure described in Section 2 and subsequently use the displacement fields for image deformation simulations as described in Section 4. Therefore it is essential that the kinematic data that is included in the cost function correctly encodes the specified material parameters. However, in explicit dynamic simulations spurious oscillations appear in the kinematic fields which arise from the spatial and temporal discretisation of the model [40–42]. These oscillations are especially prominent in the acceleration fields creating inconsistencies between acceleration and stress. In order to minimise the effect of this it is necessary to perform a parametric sweep of mesh density and damping coefficient, as described in the following section.

3.2 Mesh Convergence and Damping Selection

To ensure that the acceleration fields extracted from the explicit dynamics model are in equilibrium with the stress fields, the stress-gauge equation (equation 4) is used. Taking the average stress directly from the model and comparing this to the average stress calculated from the acceleration gives a relative error which can be minimised based on a convergence study of the mesh size and input damping coefficient. Therefore, a parametric sweep of the mesh size and the linear bulk viscosity damping coefficient was performed. Three mesh sizes were analysed ($e_s = 1\ mm$, $0.5\ mm$ and $0.2\ mm$). Additionally, ten linear bulk viscosity damping coefficients were analysed starting with the default value of 0.06 down to a damping coefficient of 0. Eight additional damping coefficient values were generated by halving the default value as follows: $0.06/2^i\ ,\ i = 1 - 8$. The different parameter combinations were compared based on the root-mean-square error (RMSE) of the average axial stress over all axial slices and all time steps of the simulation:

$$RMSE_{FE}(\overline{\sigma_{xx}}^y) = \sqrt{\frac{1}{x_n t_f}\sum_{x=x_0}^{x_n}\sum_{t=t_0}^{t_f}\left(\overline{\sigma_{xx}}^y_{FE} - \rho x \overline{a_x}^{S_0}\right)^2} \tag{10}$$

where x is an axial slice with a total of $x_n = 350$ slices along the model and t is a given output time step with a total of $t_f = 128$ output steps. The average axial stress taken from the model is denoted $\overline{\sigma_{xx}}^y_{FE}$ and the average axial stress from acceleration is given by equation 4. This error was expressed as a percentage of the maximum input compressive stress of the loading pulse (P_{max}).

The resulting error as a function of the parametric sweep variables is shown in Figure 3 for the aluminium model and the steel model with linear hardening. From these results it is clear that the mesh density has a significant effect on the results with decreasing mesh size resulting in a significantly lower error. However, if only the finest mesh is considered (see Figure 3 (b) and (d)) then the minimum error is achieved when no damping is applied. This result is expected as the applied loading pulse is smooth and the use of a plastic material model reduces the need for artificial damping in explicit simulations [40].

Based on this parametric sweep the mesh size was fixed at $0.2\ mm$ and the linear bulk viscosity damping coefficient was set to 0. Note that the linear hardening models present a 'worst case scenario' here as the transition between elasticity and plasticity is discontinuous. The same analysis was performed for the aluminium and steel models with Voce hardening giving the same optimal mesh density of $0.2\ mm$ and damping coefficient of 0.

For the chosen configuration the error between the average stress taken directly from the FE model and the stress calculated from the acceleration is shown in Figure 4 for all hardening laws. This demonstrates that the error is generally less than 1% over most axial slices and time steps. The peak error occurs at the impact edge where the load is introduced for all models at the time point when the sample begins to plastically deform. However, this error appears to be fairly localised and dissipates away from the impact edge. There is also an increase in error when the wave rebounds off the free edge caused by the sharp change of impedance. Here, one

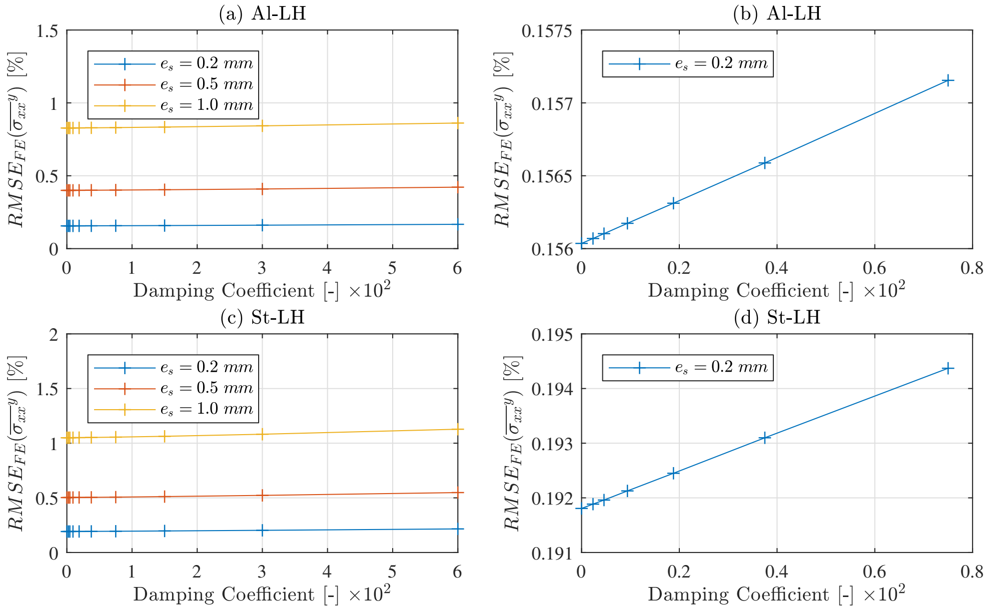

Figure 3: Convergence study results based on mesh size e_s and linear bulk viscosity damping coefficient. All results (a),(c) and zoomed in view of the region of lowest error for a mesh of 0.2 mm (b),(d).

should notice the potential of the stress-gauge equation to verify explicit FE computations and act as a tool for a convergence study.

3.3 Stress Reconstruction Validation

In order to evaluate the cost function for the SG or SB virtual fields it is necessary to calculate the stress from the strain fields using the constitutive parameters. This was achieved using a return-mapping algorithm (RMA) based on the work of de Souza Neto *et al.* [43]. This algorithm was implemented in Matlab (r2018a). In order to verify the functionality of the RMA it was applied to the strain fields extracted from the finite element models. The average axial stress calculated using the RMA was compared to the average axial stress taken directly from the finite element model. Here, the error is expressed as a percentage of the peak pressure of the loading pulse, P_{max}, as shown in Figure 5. Over most axial slices and time steps the error between the RMA and the stress taken from the model is well below 1%. However, there is a build up of error once the applied pulse begins to decrease (after $\sim 20\ \mu s$). This error builds to a maximum at the edge where the pressure pulse is applied. Close analysis of the error maps shows that a small error is introduced when the specimen begins to plastically deform. This error is carried forward by the RMA and becomes amplified once the sample begins to unload. Applying the RMA to a single element implicit calculation with unloading showed minimal error. This suggests the problem comes from the explicit FE calculation itself and not the RMA. The effect of this error on the identification procedure is investigated further in the following section.

3.4 Elasto-Plastic Identification Validation

The plastic parameters for each hardening law were identified by minimising the cost function for the SG or SB virtual fields (equations 8 and 9 respectively). For the purpose of calculating the stress from strain using the RMA the elastic parameters were fixed using the values given in Table 1. To analyse the stability of the minimisation procedure, the identification was repeated

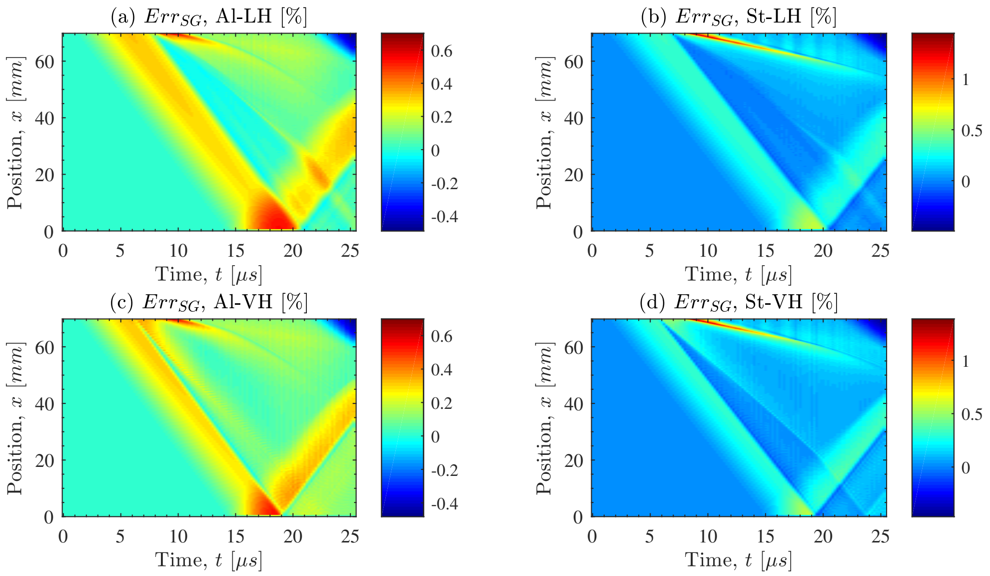

Figure 4: Percentage error between the average axial stress taken from the FE models and average axial stress calculated with the stress-gauge (equation 4) for the optimal mesh density and damping coefficient. Note that $x = 0$ is the free edge of the sample.

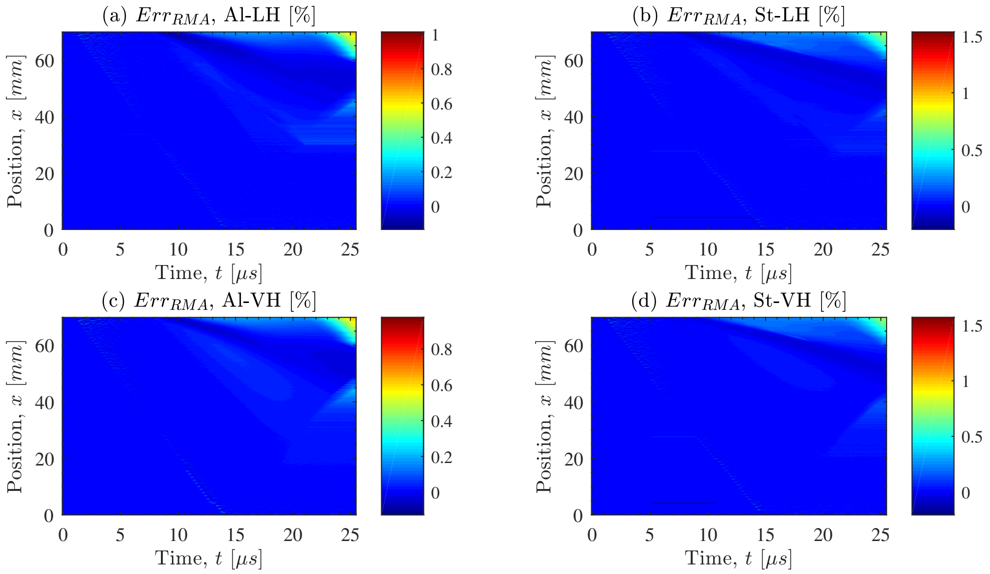

Figure 5: Percentage error between the average axial stress taken from the FE models and the average axial stress calculated with the RMA. Note that $x = 0$ is the free edge of the sample.

	Aluminium (Al)				**Steel (St)**			
	All Data		Reduced Data		All Data		Reduced Data	
Linear (LH)	SG Diff. %	SB Diff. %	SG Diff. %	SB Diff. %	SG Diff. %	SB Diff. %	SG Diff. %	SB Diff. %
σ_0	$+0.21$	$+0.07$	$+0.18$	$+0.01$	$+0.33$	$+0.06$	$+0.28$	$+0.01$
H	-1.87	-1.44	-0.97	-0.74	-1.21	-0.92	-0.59	-0.63
Voce (VH)	SG Diff. %	SB Diff. %	SG Diff. %	SB Diff. %	SG Diff. %	SB Diff. %	SG Diff. %	SB Diff. %
σ_0	$+2.00$	-1.79	$+1.97$	$+0.39$	$+1.05$	$+0.25$	$+1.02$	$+0.13$
R_0	-2.17	-1.50	-1.26	-0.84	-2.28	-1.29	-1.62	-0.80
R_{inf}	-3.22	$+4.00$	-3.41	-0.60	$+0.01$	$+0.24$	-0.28	$+0.16$
b	-3.86	$+2.19$	-3.57	-1.39	-5.51	-2.29	-4.86	-1.15

Table 2: Percentage difference between identified parameters and input reference parameters for the stress-gauge (SG) or sensitivity-based (SB) virtual fields for identifications performed directly on FE data.

three times randomising the starting point of the solver within 30% of the target values. For the SG virtual field the cost function was minimised using the Matlab function *fmincon* with the sequential quadratic programming (SQP) algorithm. For the SB virtual fields the Matlab function *lsqnonlin* was used with the Levenberg-Marquardt algorithm. Initially, the sequential quadratic programming algorithm was used for both types of virtual fields. However, this resulted in extremely long convergence times for the SB virtual fields which would not allow for the parametric sweeps which are described later in this article. For the SB virtual fields the Levenberg-Marquardt algorithm converged in a similar time to the SQP algorithm applied to the SG virtual field. As an approximate guide to solution time (using a standard desktop PC) the fastest case was the linear hardening model identified with the SG virtual field which always solved in less than 10 *minutes*. The slowest case was the Voce model identified with SB virtual fields which solved in less than 30 *minutes*. The accuracy of each algorithm for each identification method is verified in this section by applying the identification directly to finite element data.

The virtual mesh density for the SB virtual fields was set to be 14 × 14 elements and the virtual boundary conditions were set to constrain the virtual displacements at the impact edge. The identified values for this case are given in Table 2. For both types of virtual fields all data in space and time was included in the cost function for the 'All Data' condition in the table. Given that the identifications have been performed directly on FE data (with nominally perfect encoding of the material parameters), the errors are quite high with some parameters having an error on the order of several percent. It also appears that it is more difficult to identify the parameters associated with the hardening modulus than the initial yield stress. This was expected as during plastic deformation a large change in strain is required for a small change in stress. Thus, small errors on the stress can lead to large differences in hardening modulus.

Analysis of Figures 4 and 5 shows that there are errors in the FE calculation which will have an effect on the identified parameters. In order to investigate this, the data resulting in the highest error was excluded from the cost function for both types of virtual fields. Therefore, 5 axial slices of data were excluded from the free and impact edges and the last 6 time steps were excluded. Note that this is comparable to the amount of data that is excluded for processing image deformation data later in this article where a grid pitch (5 *pixels*) of data is lost on all edges of the sample (recall that the element size is $e_s = 0.2$ *mm*) Note that for the SG virtual field the slices are excluded from the cost function but the data near thee free edge of the sample is still required to calculate the surface average of the acceleration from the free edge. For the SB virtual fields excluding data on the borders of the sample requires that the virtual boundary conditions are fixed on each border where data is excluded. To be consistent with the image deformation analysis that was performed (see Section 4) the virtual displacements along all boundaries of the specimen were fixed to zero.

When the highest error regions are excluded from the cost function the error on the identified parameters is generally lower as shown in Table 2 for the 'Reduced Data' condition. The improvement is more significant for the hardening modulus parameters than for the yield stress which already had a low error. Overall, the error is mostly below 2% apart from the identification of the Voce model with the SG virtual field. This is probably because this simple virtual field is not rich enough to accurately discriminate all four parameters of the model. This is evident when the results for the SG virtual field are compared with the SB virtual fields which have much lower errors for the Voce model; confirming the superiority of the SB virtual fields for models with a larger numbers of parameters, as already noticed in [44]. It is also worth mentioning that the errors here are numerical and mostly result from the explicit FE calculation.

4 Error Quantification using Image Deformation

Having validated the elasto-plastic identification routines on finite element data, the displacement fields from the FE model can be used to create a series of synthetic images. The advantage of using FE data for creating synthetic images is that, unlike experimental data, the constitutive law encoded in the images is known *a-priori* and the input parameters to the FE model serve as reference values for error analysis. The purpose of this analysis is to understand the propagation of experimental errors through the full-field measurement process and inverse identification method. The general procedure for this type of synthetic image deformation analysis is discussed in [35, 36, 45] for digital image correlation and in [23, 25, 37, 38, 46] for the grid method.

This section begins by briefly describing the procedure for generating synthetic images before applying the procedure to noise free images to analyse the systematic error resulting from the temporal and spatial resolution of the camera. A sweep of the smoothing parameters is then performed for noise free and noisy images to analyse the resulting systematic and random errors for the identified parameters.

4.1 Image Deformation Procedure

The specific procedure used for generating synthetic grid images in this work is described in detail in [23, 25, 46] so it is only briefly recalled here. Consider the equation describing a two dimensional sinusoidal grid with grey level intensity $G(x, y)$:

$$G(x,y) = 2^b \left[I_0 + \frac{\gamma}{4} \left(1 + cos\left(\frac{2\pi x}{p} \right) \right) \left(1 + cos\left(\frac{2\pi y}{p} \right) \right) \right] \tag{11}$$

where b is the number of bits encoding the image, I_0 is the mean light intensity, γ is the amplitude of the grid pattern and p is the pitch of the grid. Note that I_0 and γ are expressed as fractions of the dynamic range, for example $I_0 = 0.5$ and $\gamma = 0.25$ gives a grid with a mean intensity of 50% of the dynamic range and amplitude of 25% of the dynamic range. To create deformed grid images using equation 11 the x and y coordinates are substituted for the deformed location of each pixel of the grid as follows: $x = x_0 + u_x$ and $y = y_0 + u_y$ where x_0, y_0 is the initial undeformed position of the pixel and u_x, u_y are the displacements taken from the finite element model interpolated onto the pixel locations. The parameters of the synthetic images were set to

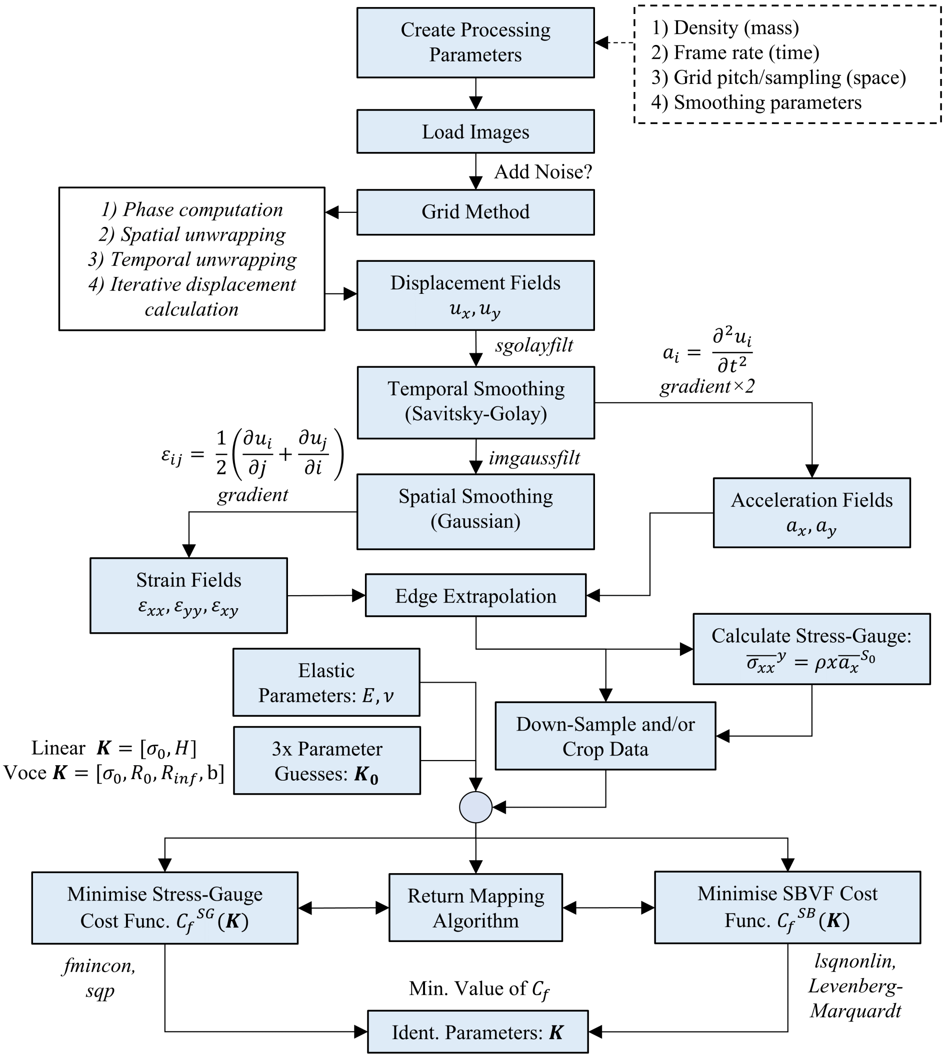

Figure 6: Flow chart showing the data processing procedure from raw grid images through to identified elasto-plastic parameters.

be representative of the experimental data: $I_0 = 0.5$, $\gamma = 0.2$, and a grid pitch of $p = 0.9\ mm$ with a sampling of $pxpp = 5\ pixels/period$. The remaining parameters were set to replicate the Shimadzu HPV-X camera that was used for the experimental campaign: $b = 10$, frame rate of $5\ Mfps$ and a pixel array size of $400 \times 250\ pixels$.

4.2 Data Processing and Inverse Identification

Once a series of synthetically deformed grid images is obtained they are processed exactly like experimental data. This section briefly describes this procedure beginning with the extraction of the displacement fields using the grid method through to implementing the inverse identification. The data processing method used here follows the general procedure for processing IBII data as outlined in [46]. An overview of the specific data processing procedure developed here for elasto-plasticity is given in Figure 6 and is explained in the rest of this section.

In this work and previous studies using the IBII test the grid method has been used as it offers an improved trade-off between spatial and measurement resolution when compared to

DIC [47]. A detailed review of the grid method theory and applications is given in [6]. The grid method Matlab code used in this work was developed by Grediac *et al.* [6] and can be freely downloaded[1]. All additional data processing code can be found in the digital dataset described at the end of this article.

After extracting the full-field displacements from the images using the grid method the next step is to apply temporal smoothing. In this study a 2nd order Savitsky-Golay filter was used to smooth the displacement fields in time (using the Matlab function *sgolayfilt*). The size of the temporal smoothing kernel T_{ks} was set to be an odd integer number of frames. The temporally smoothed displacements were then used to calculate the acceleration using the centred finite difference method twice (once to obtain velocity and again to obtain acceleration). Numerical differentiation with the centred finite difference algorithm was implemented using the *gradient* function in Matlab. The temporally smoothed displacements were then smoothed in space using a Gaussian filter with a kernel size, S_{ks}, specified as an odd number of pixels (using the Matlab function *imgaussfilt*). The standard deviation of the Gaussian kernel was set based on the kernel size using the default value in Matlab given by the equation: $S_{ks} = 2\lceil 2SD \rceil + 1$ where SD is the standard deviation of the kernel and $\lceil \ \rceil$ denotes the ceiling function. Note that in the following sections (Section 4.3 and 4.4) a parametric sweep of the spatial and temporal smoothing kernel sizes is performed to identify the optimal configuration for processing the experimental data. Hence, no specific kernel size is given here. Following spatial smoothing the strains were calculated using a centred finite difference algorithm (again using the Matlab function *gradient*).

An important consideration when dealing with kinematic data derived from full-field measurements is how to account for the data that is lost along the borders of the sample. Previous work has shown that simply padding the missing edge data by replication results in improved identification with the VFM [45]. Therefore, this simple approach has been adopted here with the padding being performed directly on the resultant kinematic fields (*i.e.* acceleration and strain) over the missing grid pitch of data on each edge.

Note that in previous studies by the authors the temporal and spatial smoothing procedures have been intentionally decoupled (*i.e* only temporal smoothing for acceleration and only spatial smoothing for strains), see for example [22, 23, 25]. Here it is beneficial to apply temporal smoothing to the strains as the RMA is calculated based on the strain increment which is more stable in the presence of noise when strains are temporally smoothed.

Once the kinematic fields have been calculated they are used to minimise the cost function for either the SG or SB virtual fields. For the purpose of calculating the stress from strain using the RMA the elastic parameters were taken as the ones input into the FE model (see Table 1). There are several additional considerations when applying the elasto-plastic identification procedure to the kinematic fields derived from images. The first of these results from the data that is lost on the edges of the sample. The second problem results from edge effects coming from the differentiation scheme and from the temporal/spatial smoothing filters. Fortunately, it is not required to include all spatial data and time steps in the minimisation of the cost function. Thus, the data corrupted by edge effects were intentionally excluded from the cost function where possible. In time, a number of frames equal to $\lceil T_{ks}/2 \rceil + 6$ was excluded from the end of the data. For the SG virtual field, a number of axial slices equal to $\lceil S_{ks}/2 \rceil + pxpp$ were excluded from the free and impact edges, where $pxpp$ is the number of pixels used to sample the grid (in this case 5). It was found that a minimum of $2pxpp + 1$ pixels needed to be excluded from the identification to ensure that all corrupted data was removed from the cost function. Therefore, if $\lceil S_{ks}/2 \rceil + pxpp$ was less than $2pxpp + 1$ a total of $2pxpp + 1$ pixels were excluded. For the SB virtual fields the same spatial exclusion rule was applied. However, for the SB virtual fields data

---

[1] http://www.thegridmethod.net/code

Temporal Kernel Size, T_{ks} $[frames]$	$0, 5, 11, 15, 21, 25, 31$
Spatial Kernel Size, S_{ks} $[pixels]$	$0, 11, 21, 31, 41, 51, 61$

Table 3: Smoothing kernel sizes used in the parametric sweep.

was excluded from all edges. The virtual boundary conditions for the SB virtual fields were also set to constrain all edges of the sample where data was excluded.

The minimisation of the cost function for both types of virtual fields was performed using the same Matlab functions that were used for the validation on finite element data (see Section 3.4). For all identifications, three random starting points were used for the minimisation procedure and the identified parameters were taken as the ones returning the overall minimum value of the cost function.

4.3 Error Analysis on Noise Free Images

In this section a series of deformed grid images without noise are used to evaluate the systematic error for each case. A parametric sweep of the temporal and spatial smoothing kernel sizes was performed using the smoothing kernel sizes given in Table 3. In general the systematic error is evaluated by comparing the identified parameters to the reference ones originally input into the FE model and plotting the percentage error. The systematic error taken from images without noise is denoted Err^0_{sys}. It becomes more difficult to visualise the error maps when material models have more than two parameters. In this case it can be easier to incorporate all parameters into a single error metric by analysing the root-mean-square (RMS) error on the identified 1D stress-strain curve. The RMS error on the 1D stress-strain curve is compared up to 5% total strain as this is the approximate maximum strain observed in the experimental data. The RMS error on the 1D stress-strain curve is then normalised by the maximum stress and expressed as a percentage. The RMS error using the 1D stress-strain curve is denoted using the short hand 'SSC' for the remainder of this article, for example: $Err^0_{sys}(SSC)$ is the systematic error without noise calculated using the RMS error on the 1D stress-strain curves .

4.3.1 Linear Hardening Results: No Noise

In the interest of reducing computational time and increasing the strain increment for the RMA the data can be down-sampled such that every third frame is included in the cost function. This analysis was performed for each case considered here and it was found that this had a minimal effect on the resulting systematic error so the results shown in this section and for the rest of the paper are only for the down-sampled case. Note that the down-sampling only occurs for the data input into the cost function with the intermediate frames still contributing to the temporal smoothing and temporal differentiation procedures. The systematic error maps for the case where all frames are used in the cost function are included in the digital dataset described at the end of this article.

The systematic error on the identified linear hardening parameters with the SG virtual field is shown in Figure 7. In this figure the minimum absolute error for all cases is shown using a red cross. This convention is adopted throughout the remainder of the article with a red cross being used to represent the minimum absolute error on all error maps. The systematic error resulting from the camera resolution is remarkably low given that the simulated camera only has 400 × 250 $pixels$. The results also show that the identified parameters are most sensitive to spatial smoothing and that the systematic error generally increases with smoothing, as expected. The hardening modulus shows the most sensitivity to smoothing for both the aluminium and steel cases whereas the yield stress shows a similar pattern and error magnitude

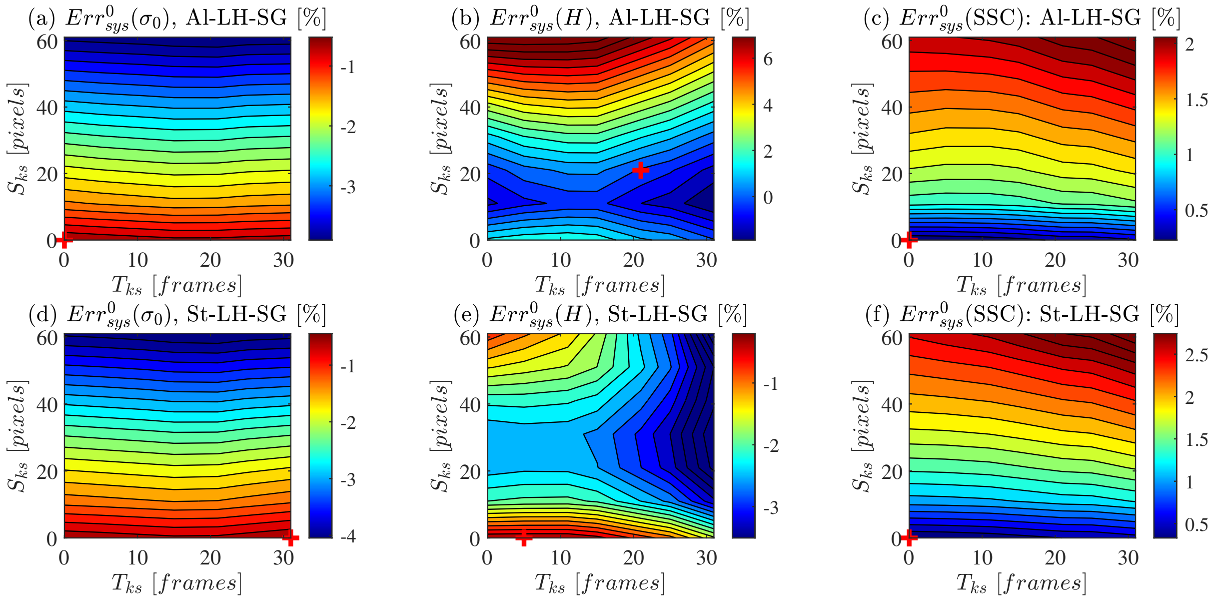

Figure 7: Systematic error when using the stress-gauge (SG) virtual field as a function of smoothing kernel size. Results are given for the aluminium (Al) and steel cases (St) using the linear hardening model (LH) with no noise added to the images. For this case only every third frame is used in the cost function.

for both materials. The difference in the behaviour of the hardening modulus does not result in a significant difference in the RMS error on the 1D stress-strain curve (see Figure 7 (c) and (f)). This result shows that the systematic error for the no noise case is low and insensitive to the material being considered when using the SG virtual field.

The same analysis was performed for the SB virtual fields with the associated systematic error maps given in Figure 8. In a similar manner to the SG virtual field, the systematic error maps for the SB virtual fields generally show increasing systematic error with increased smoothing. The hardening modulus also has a larger error than the yield stress. However, the systematic error coming from the camera resolution is still remarkably low, being typically less than one percent when the SB virtual fields are used. Overall, comparison of the results using the 1D stress-strain curve error maps from the SG virtual field with the SB virtual fields shows that the systematic error is slightly lower for the SB virtual fields. However, given that the systematic error for all cases is at most a few percent it is not certain if this is significant.

In order to obtain a more intuitive sense of how the RMS error translates to the 1D stress-strain curve it is useful to analyse the stress-strain curves for low and high systematic errors. This is shown in Figure 9 for the linear hardening case. The identified stress-strain curve is almost indistinguishable from the reference curve when no smoothing is applied. This case corresponds to an RMS error of $\sim 0.5\%$ or less. For the case where a large amount of smoothing is applied to the aluminium model the RMS error is 2.3% when the identification is performed with the SG virtual field (see Figure 9 (a)). When performing the identification with the SB virtual fields, as in Figure 9 (c), the RMS error is 0.7%. For the steel case the RMS error on the stress-strain curve is $\sim 2.6\%$. Qualitative analysis of all stress-strain curves shown in Figure 9 suggests that a systematic error of few percent or less on the 1D stress-strain curve is desirable to represent the material response accurately. The next section considers the same systematic error analysis in the absence of noise for the Voce hardening law.

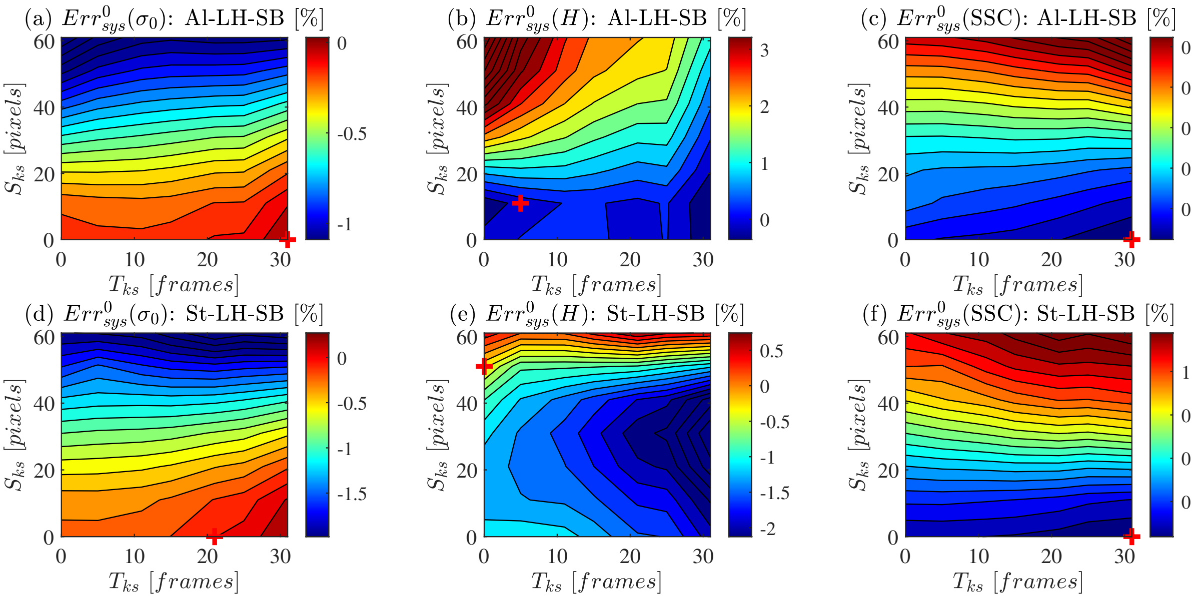

Figure 8: Systematic error when using the sensitivity-based (SB) virtual fields as a function of smoothing kernel size. Results are given for the aluminium (Al) and steel cases (St) using the linear hardening model (LH) with no noise added to the images. For this case only every third frame was included in the cost function.

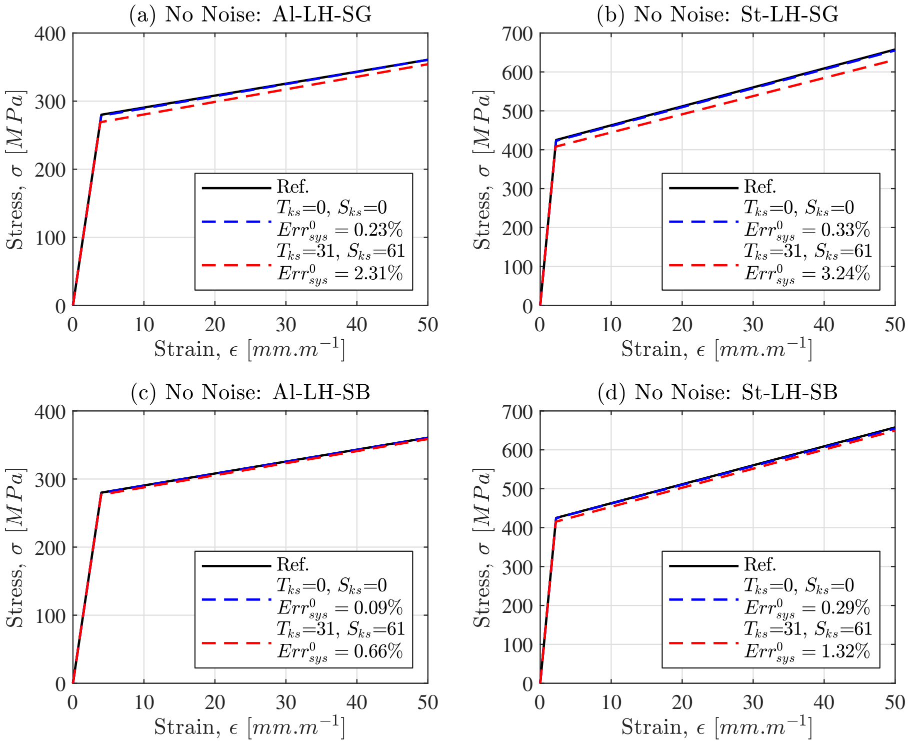

Figure 9: Comparison of the 1D stress-strain curves for the no noise smoothing sweep showing a curve with low systematic error and a curve with high systematic error. Results are shown for the linear hardening aluminium (Al-LH) and steel (St-LH) with identifications performed with the stress-gauge (SG) or sensitivity-based (SB) virtual fields.

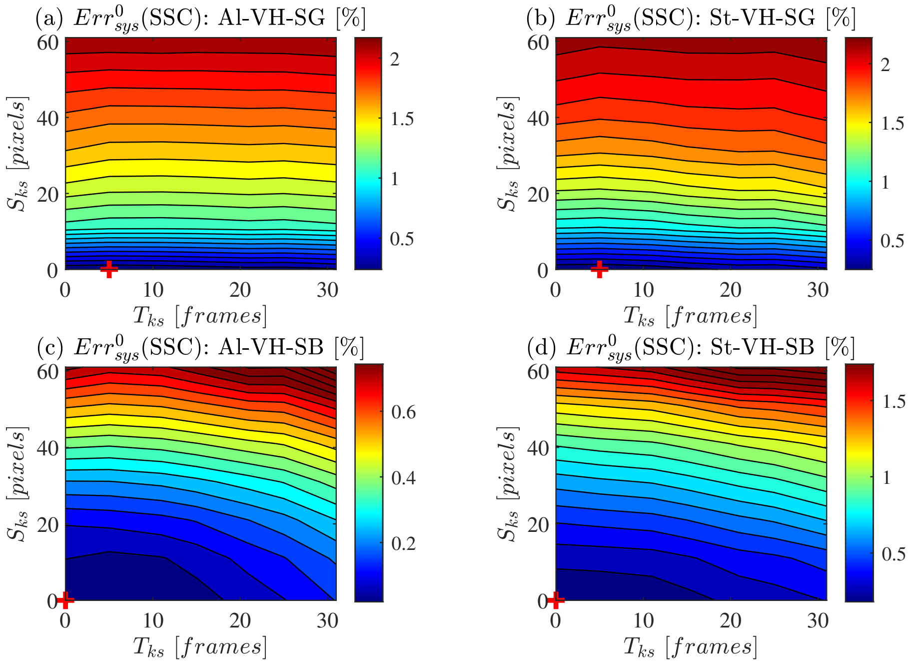

Figure 10: Systematic error without noise for the Voce hardening law (VH) using either the stress-gauge (SG) virtual field or the sensitivity-based (SB) virtual fields.

4.3.2 Voce Hardening Results: No Noise

Given that there are four parameters to analyse for the Voce model it is simpler to visualise the combined systematic error based on the 1D stress-strain curve. Therefore, the systematic error based on the 1D stress-strain curve is shown in Figure 10 for both types of materials and virtual fields. Analysis of this figure shows that the resulting systematic error for all cases is quite low (typically less than 2%). This means that both types of virtual fields are able to successfully identify the Voce hardening law even in the presence of the systematic errors coming from the camera (*i.e.* the number of pixels, frame rate and digitisation). All identification cases show the expected trend with increasing systematic error with increasing smoothing kernel size. However, SB virtual fields show slightly more of an effect from temporal smoothing. The overall error magnitude is generally lower for the SB virtual fields. This result is not surprising as the SB virtual fields create tailored virtual fields which focus on the area where each of the four model parameters are activated leading to an improved identification.

Here it is also useful to analyse how the RMS error maps shown in Figure 10 translate into the overall shape of the 1D stress-strain curve for the Voce model. The 1D stress-strain curves for the cases of no smoothing (low systematic error) and maximum smoothing (high systematic error) are shown in Figure 11. For all cases considered in this section the systematic error resulting from the camera resolution is low. The next step is to perform the same analysis in the presence of noise, as is discussed in the next section.

4.4 Error Analysis on Noisy Images

Now we consider the same sweep of the smoothing parameters as given in Table 3, but this time the images are polluted with grey level noise before processing. In order to replicate the noise observed in the experiment, static image sequences of each experimental specimen were analysed giving a standard deviation of 0.4% of the whole dynamic range for the grey level noise. It is

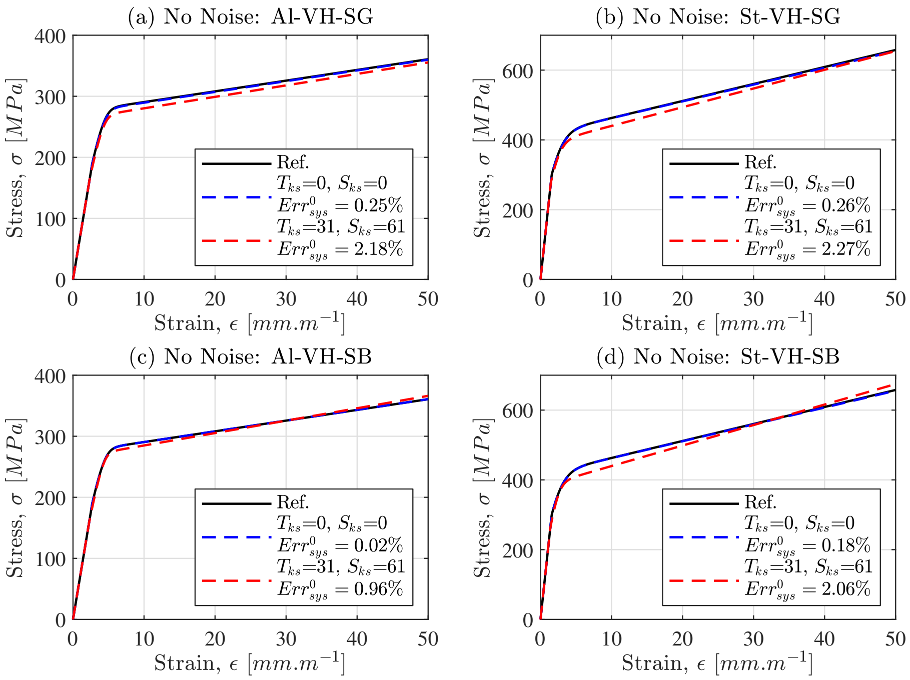

Figure 11: Comparison of the 1D stress-strain curves for the no noise smoothing sweep showing a curve with low systematic error and a curve with high systematic error. Results are shown for the Voce hardening aluminium (Al-VH) and steel (St-VH) models with identifications performed with the stress-gauge (SG) or sensitivity-based (SB) virtual fields.

worth noting that though the noise is heteroscedastic (standard deviation increases with grey level value), it is assumed homoscedastic here.

When processing noisy images it is necessary to perform the identification several times for different independent copies of noise. Thus, the identification was performed on thirty copies of noise for each combination of smoothing kernel sizes. The systematic error was determined by comparing the median of the identified parameters over thirty identifications with the reference parameters. To differentiate this from the systematic error determined without noise (Err^0_{sys}) the systematic error identified from the median over the thirty copies of noise is denoted Err^+_{sys}. If there is no noise-induced bias then the systematic error with and without noise should be the same. The random error Err_{rnd} is taken to be median absolute deviation (MAD) over the thirty identifications. Non-normal statistical measures were chosen here as they are robust in the presence of outliers, making it easier to distinguish the most likely solution for the Voce model which can have uniqueness issues[2].

In order to find the optimal trade off between the random and systematic errors the 'total error' is used. This is defined as: $Err_{tot} = |Err^+_{sys}| + 2Err_{rnd}$. The systematic, random and total error for the 1D stress-strain curve was calculated in a similar manner by analysing the RMS error for all thirty stress-strain curves. The systematic error ($Err^+_{sys}(SSC)$) was taken as the median RMS error and the random error ($Err_{rnd}(SSC)$) was taken as the median absolute deviation of the RMS error over all thirty stress-strain curves. The total error was defined using the same equation defined previously. All error metrics in the following section are normalised by

---

[2] For the linear hardening case the results for defining the error with the mean and SD are similar to the median and MAD. For the Voce model there are some cases where the b parameter tends to infinity for certain copies of noise so the mean and SD are heavily skewed by this value. This makes the median and MAD more robust measures of the most likely outcome.

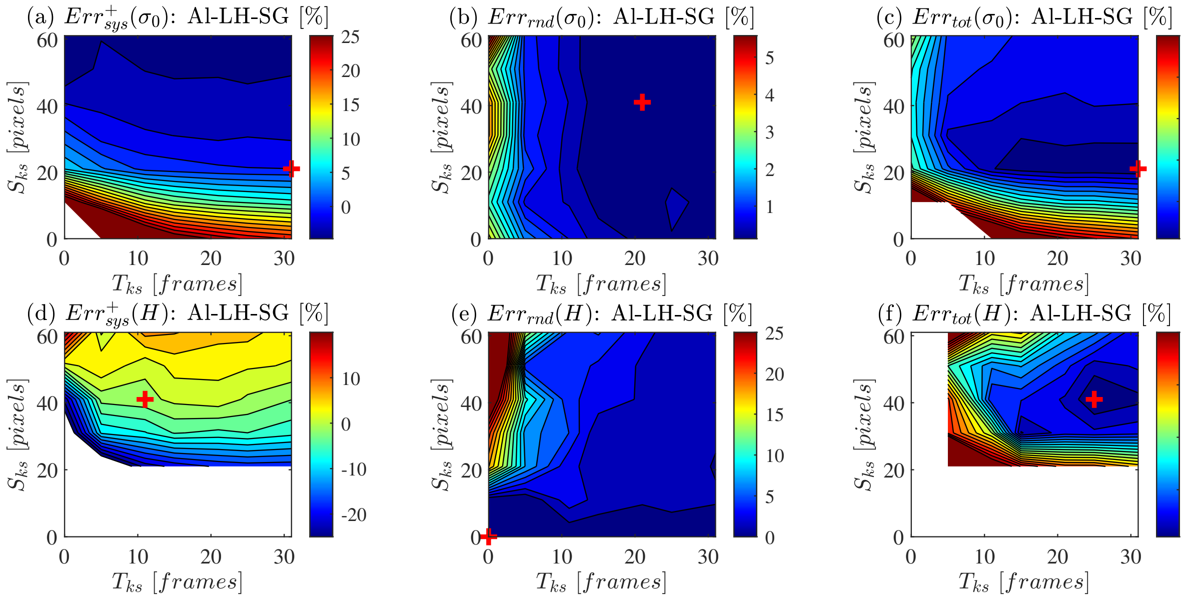

Figure 12: Identification error maps using the stress-gauge (SG) virtual field on noisy data for the aluminium linear hardening case (Al-LH). Note that data points above 50% error have been omitted for clarity.

the reference material parameter and expressed as a percentage apart from the 1D stress-strain curve which is normalised by the maximum stress.

4.4.1 Linear Hardening Results: With Noise

The resulting random, systematic and total errors for the linear hardening aluminium case are shown in Figure 12. Note that in Figure 12 data points with a large error (in this case greater than 50% error) have been removed so that regions resulting in a reasonable identification are clearer. Comparing the predicted systematic error for the no noise case (see Figure 7) and the noisy case shown here indicates that there is a significant noise-induced bias on the identification. The cause of this bias is investigated in the following section (Section 4.4.2), for now the focus is on analysis of the parametric sweep and selection of optimal smoothing parameters. The noise induced bias is very large for smoothing kernel sizes below $T_{ks} = 11\ frames$ and $S_{ks} = 11\ pixels$.

Figure 12 shows that the noise-induced bias is larger for the hardening modulus leading to a region of high systematic error below a spatial smoothing kernel size of $S_{ks} = 21\ pixels$. For this same region the random error appears to drop significantly for the hardening modulus. However, this is misleading as the identifications in this region tend to return a hardening modulus of 0 (note that the hardening modulus was constrained to be larger than 0). The yield stress shows a similar trend to the hardening modulus with a large systematic error for spatial smoothing kernel sizes below $S_{ks} = 21\ pixels$. The random error on the yield stress is generally quite low, being under 2% over most smoothing kernel sizes as long as a small amount of temporal smoothing is applied. An interesting trend shown for both parameters is that the systematic error is mostly dependent on the spatial smoothing kernel size whereas the random error is most sensitive to the temporal smoothing kernel size. This creates a region in the top right corner of the total error maps where there is a good compromise between the random and systematic errors. The error maps for the linear hardening steel case show similar trends to the linear hardening aluminium case shown in Figure 12. Therefore, they are not shown here but can be found in the digital dataset described at the end of this article.

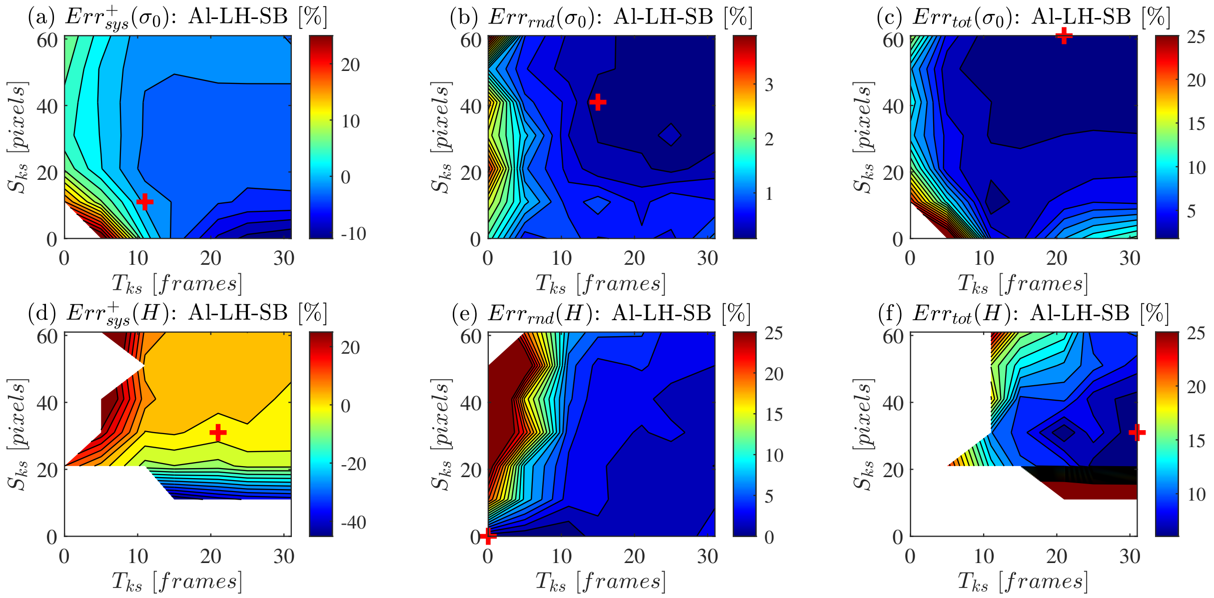

Figure 13: Identification error maps using the sensitivity-based (SB) virtual fields on noisy data for the aluminium linear hardening case (Al-LH). Note that data points above 50% error have been omitted for clarity.

The error maps for the identification of a linear hardening law using the SB virtual fields are shown in Figure 13 for the aluminium model. Comparing this to the results for the SG virtual field shows that the overall trends are similar. Specifically, there is a large noise-induced bias which has a more significant effect on the identification of the hardening modulus. The random error also seems to be reduced by temporal smoothing and the top right quadrant of each map shows a valley where the total error tends towards a minimum.

Analysis of the total error maps suggests that a spatial smoothing kernel size above 21 *pixels* and a temporal smoothing kernel size above 11 *frames* is needed to minimise the total error for both linear hardening parameters. However, to select the smoothing kernel sizes giving the best overall trade-off for both hardening parameters it is useful to analyse the total error calculated using the 1D stress-strain curve. This is shown in Figure 14 for the aluminium and steel cases with the identification performed with the SG virtual field and the SB virtual fields. In Figure 14 (c) the absolute minimum error for the aluminium identification using the SB virtual fields occurs at the highest spatial smoothing kernel. For this case we notice that the area over which the error is low is reasonably large with the next smallest error occurring at a spatial smoothing kernel of 51 *pixels* and a temporal smoothing kernel of 15 *frames*. The difference in total error between these cases is only 0.003%. It is desirable to minimise the size of the smoothing kernels to reduce the amount of data excluded from the edges so for this case a spatial smoothing kernel of 51 *pixels* and temporal smoothing kernel of 15 *frames* is used. For the remaining cases the absolute minimum error is more clearly defined so the smoothing kernels are taken directly from the error maps.

The optimal smoothing kernel sizes for each case are summarised in Table 4 along with the identified parameters and associated error. In this figure all cases with a spatial or temporal smoothing kernel of 0 have been excluded to avoid the region of large noise induced bias. An interesting general trend in Figure 14 is that there is a large region in the top right quadrant of the map over which the total error on the 1D stress strain-curve is less than 3% for both materials.

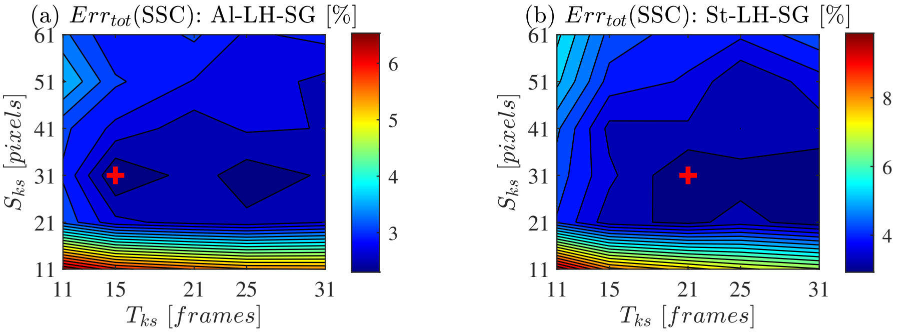
(a) Err_{tot}(SSC): Al-LH-SG [%]

(b) Err_{tot}(SSC): St-LH-SG [%]

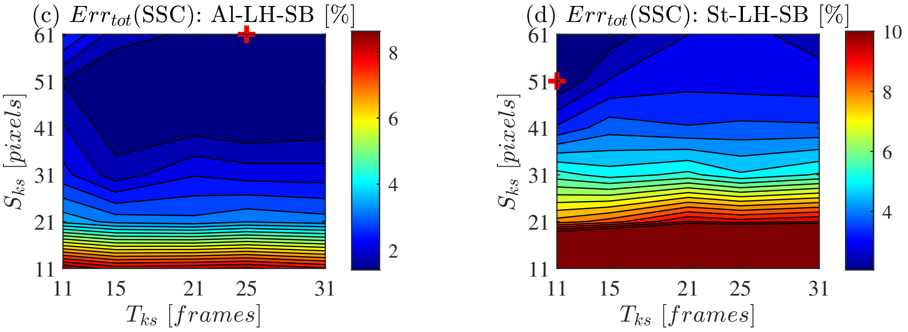
(c) Err_{tot}(SSC): Al-LH-SB [%]

(d) Err_{tot}(SSC): St-LH-SB [%]

Figure 14: Total error on the 1D stress-strain curve for the stress-gauge (SG) virtual fields and the sensitivity-based (SB) virtual fields applied to the linear hardening aluminium (Al-LH) and steel (St-LH).

	Aluminium (Al)		Steel (St)	
	Stress-Gauge (SG)	Sensivity-Based VFs (SB)	Stress-Gauge (SG)	Sensivity-Based VFs (SB)
T_{ks} $[frames]$	15	15	21	11
S_{ks} $[pixels]$	31	51	31	51
Err^{+}_{sys}(SSC) [%]	1.59	0.75	2.11	1.01
Err_{rnd}(SSC) [%]	0.36	0.33	0.41	0.52
Err_{tot}(SSC) [%]	2.30	1.40	2.93	2.05
$\sigma_0(med/ref)$	0.98	0.98	0.99	0.99
$\sigma_0(MAD/ref)$ [%]	0.14	0.38	0.31	0.62
$H(med/ref)$	0.97	1.06	0.91	1.02
$H(MAD/ref)$ [%]	1.48	3.52	1.14	3.68

Table 4: Optimal smoothing parameters for the linear hardening case using the stress-gauge (SG) or sensitivity-based (SB) virtual fields.

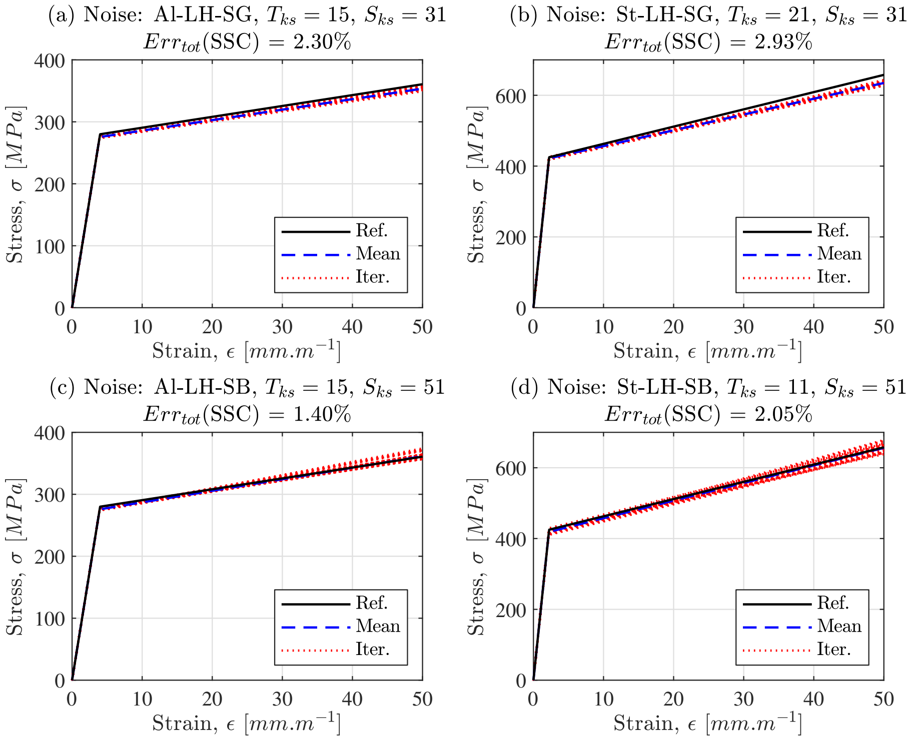

Figure 15: Comparison of the 1D stress-strain curves for the noisy smoothing sweep on the linear hardening models. All thirty identifications are shown for the case where the optimal smoothing parameters are used giving an indication of the scatter and mean response.

To interpret the total error maps for the 1D stress-strain curves shown in Figure 14 it is useful to analyse the distribution of all thirty identified stress-strain curves when using the optimal smoothing parameters given in Table 4. This is shown in Figure 15 for all linear hardening cases. This confirms that there is no significant difference between the identifications for the aluminium or steel cases.

Interestingly, the results in Figure 14 and Table 4 show that there is not a large difference between the two types of virtual fields when considering a simple linear hardening model. Both types of virtual fields tend to underestimate the yield stress. This is possibly due to spurious plastic strain caused by noise when the material is close to the elastic limit. The SG virtual field also underestimates the hardening modulus whereas the SB virtual fields tend to overestimate the hardening modulus. For the SB virtual fields the combination of under predicting the yield stress and over predicting the hardening modulus leads to a lower total error when compared to the SG virtual field, as is shown in the stress-strain curves in Figure 14. The SB virtual fields seem to require slightly more spatial smoothing but this difference is probably not significant. Another general observation from Figure 14 is that the SB virtual fields exhibit slightly more scatter but the overall mean curve is closer to the reference response. Having considered the linear hardening model for both materials and both types of virtual fields it is necessary to analyse the source of the noise-induced bias on the identification procedure.

4.4.2 Analysis of Noise-Induced Bias

In order to investigate the cause of the noise-induced bias the two terms in the SG virtual field cost function (equation 8) were analysed separately *i.e.* the average stress calculated from the strain using the constitutive parameters and the average stress calculated from the acceleration.

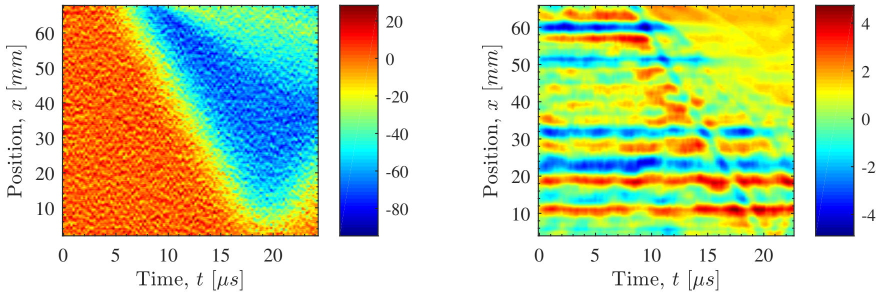
(a) $Err_{ID}(\overline{\sigma_{xx}}^y)$ RMA, Al-LH Unsmoothed [%]

(b) $Err_{ID}(\overline{\sigma_{xx}}^y)$ RMA, Al-LH Smoothed [%]

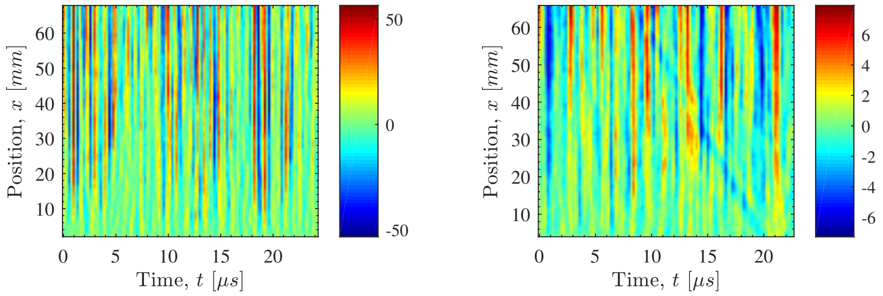
(c) $Err_{ID}(\overline{\sigma_{xx}}^y)$ SG, Al-LH Unsmoothed [%]

(d) $Err_{ID}(\overline{\sigma_{xx}}^y)$ SG, Al-LH Smoothed [%]

Figure 16: Error between the average stress calculated using the kinematic fields from the FE model and from the image deformation simulation for the linear hardening aluminium model (Al-LH). The smoothed case uses the optimal parameters given in Table 4.

The advantage of using image deformation data here is that the average stress from each term can be compared to what is actually encoded in the FE model. Here the focus is on linear hardening for the aluminium model as the resulting analysis is similar for all other cases.

First we define the percentage error between average stress calculated using image deformation data ($\overline{\sigma_{xx}}^y_{ID}$) and the average stress from the FE model ($\overline{\sigma_{xx}}^y_{FE}$) as follows:

$$Err_{ID}(\overline{\sigma_{xx}}^y) = -\frac{\overline{\sigma_{xx}}^y_{ID} - \overline{\sigma_{xx}}^y_{FE}}{P_{max}} \times 100 \tag{12}$$

where the average stress $\overline{\sigma_{xx}}^y_{ID}$ is calculated using either the RMA or the stress-gauge equation. The negative sign is required to make the sign of P_{max} consistent with the sign of the average stress terms which are negative to indicate compression (see Figure 2 for the definition of P_{max}). Figure 16 shows the error between the image deformation simulation and the stress taken from the FE model for the unsmoothed and the optimal smoothing case ($S_{ks} = 31\ pixels$ and $T_{ks} = 15\ frames$). The error maps shown in Figure 16 have been cropped in space and time according to the data exclusion rules for the SG virtual field cost function as outlined in the data processing section (Section 4.2).

There is a clear pattern in the error map for the average stress calculated using the RMA when comparing the unsmoothed Figure 16 (a) and smoothed cases Figure 16 (b). The addition of noise causes the RMA to undershoot the average stress significantly. This is caused by spurious elastic unloading in the presence of noise. In order to illustrate this consider the strain noise floor which can be calculated by taking the standard deviation of the strain for a series of static noisy images. Applying this analysis to the case of no smoothing gives a strain noise floor of 2.75 $mm.m^{-1}$. For uni-axial loading the stress associated with this strain is given by: $\sigma_{xx} = E\epsilon_{xx} = 191\ MPa$. Therefore, the strain noise can cause a large elastic unloading leading the RMA to undercut the peak stress.

The error on the average stress calculated with the stress-gauge equation (Figure 16 (c) and (d)) shows a different pattern to the RMA. For this case vertical streaks are observed in the noise pattern with a low error near the free-edge. The low error near the free-edge results from the x variable in the stress-gauge (equation 4) which reduces the contribution of noise near the free edge. The vertical streaks along the position axis are due to the cumulative surface average that is performed from the free edge to the point x where any bias in the noise pattern is carried forward into the subsequent slices. This is illustrated on a simple example in the appendix where the only error comes from noise. Therefore, the effect of noise on the RMA leading to spurious elastic unloading is the main cause of the noise-induced bias on the parametric sweep results presented in the previous section.

Interestingly, the percentage error for the RMA and the stress-gauge is comparable for the optimally smoothed case at approximately 5%. This would suggest that comparison of the percentage errors for the stress-gauge and RMA to each other and to an approximate error of 5% could be used to inform the choice of smoothing parameters. The analysis used here has the significant advantage that the RMA only needs to be evaluated once rather than performing the minimisation procedure for many copies of noise which drastically reduces the computational time. In the future it should be possible to use this quick analysis technique to narrow the range of smoothing parameters that are analysed in the parametric sweep.

In order to make these results more transferable to other cameras in the future it is useful to consider how this translates into a signal to noise ratio for the strain increment observed in the test. The simple rectangular geometry used here results in a test where the axial strain component is dominant so we only consider the 'x' strain component. To begin with, the case where all frames are included in the analysis is considered (*i.e* no downsampling). In order to have an idea of the strain increment 'signal' in the test we consider the mean strain increment over the portion of the test where and when plastic deformation occurs. This begins at 8.2 μs and the plastic front propagates over approximately 50% of the specimen length from the impact edge so we take the mean strain increment over this region giving $-0.100\ mm.m^{-1}$. Now we consider the noise floor on the strain increment. For the case where no smoothing is applied the noise floor for the axial strain increment is 2.73 $mm.m^{-1}$. For the optimally smoothed case the noise floor for the strain increment drops significantly to 0.011 $mm.m^{-1}$. Thus, the absolute value of the signal to noise ratio for the unsmoothed case is ~ 0.04 and for the smoothed case is ~ 8.8. We can now extend the analysis to the case of down-sampling the data by taking every third frame. This increases the mean strain increment to $-0.302\ mm.m^{-1}$ with no effect on the noise floor (recall that all frames are still used in the temporal smoothing procedure) which approximately triples the signal to noise ratios given previously. The cost of down-sampling the data is usually attributed to an increase in systematic error. However, for the test configuration used here this effect was minimal.

4.4.3 Voce Hardening Results: With Noise

A similar sweep of smoothing parameters with noisy images is considered for the Voce hardening law. Here the analysis is limited to the total error for each of the model parameters as well as the total error taken from the 1D stress-strain curve. Also, as there is considerable interaction between the σ_0 and R_{inf} parameters for the Voce model, only the sum of these two parameters is given as: $\sigma_{YS} = \sigma_0 + R_{inf}$. The total error maps for the Voce model when using the SG virtual field are given in Figure 17. Here we observe that all parameters are influenced by the noise-induced bias when low amounts of smoothing are applied. Therefore, the parametric sweep for both cases has been limited to only consider minimum smoothing kernel sizes of $T_{ks} = 11\ frames$ and $S_{ks} = 11\ pixels$.

The results in Figure 17 show that overall patterns in the error maps are similar for both materials considered. Analysing just the sum of parameters associated with yielding (σ_{YS})

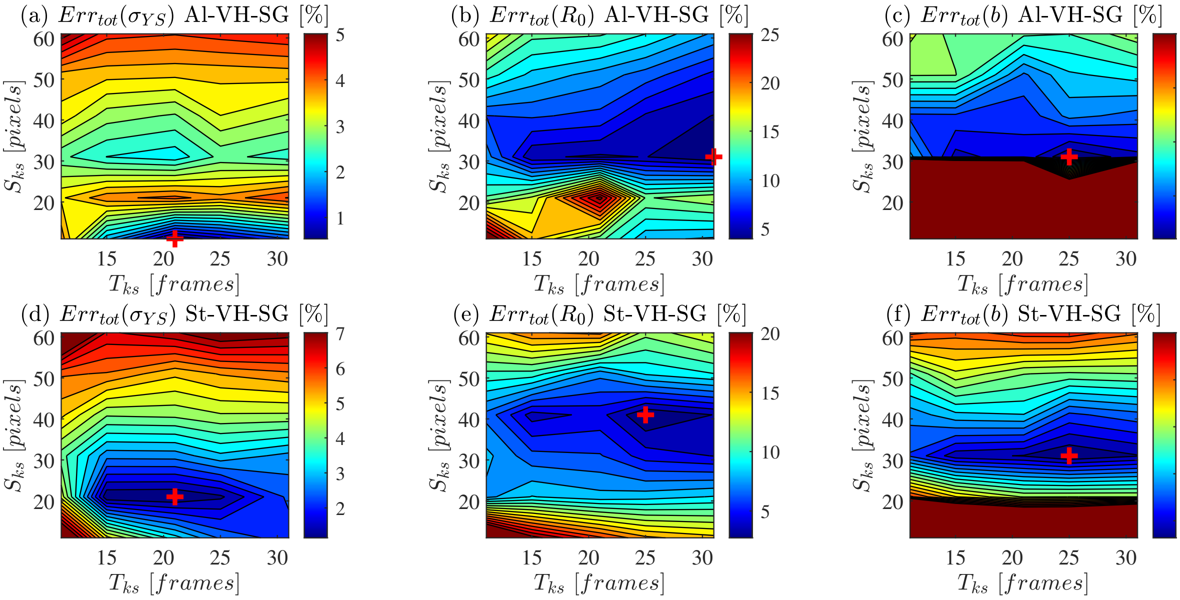

Figure 17: Total error maps for the Voce hardening (VH) law when using the stress-gauge (SG) virtual field for the identification. Results on the left show the aluminium (Al) case and results on the right show the steel (St) case.

shows that the total error is generally less than 5% as long as the region of noise induced bias is avoided and extremely large smoothing kernels are not used. Again, we observe the same trend as shown by the linear hardening model with the hardening modulus parameter being more difficult to identify. However, both materials exhibit a large region over which the total error on the long term hardening modulus is less than 10%. Finally, the region over which the curvature parameter, b, returns a reasonable error is small. This result is expected as the Voce model is not particularly sensitive to the b parameter with an order of magnitude difference being required to significantly alter the shape of the stress-strain curve. Analysis of the error maps shows that for the b parameter a minimum spatial smoothing kernel of 31 *pixels* is required. For spatial smoothing kernels below this value the b parameter tends towards infinity and the Voce model effectively collapses to a linear model (hence the region of high error). This problem also seems to be more pronounced for the aluminium case. Therefore, the search for the optimal smoothing kernels based on the RMS error on the 1D stress-strain curve is limited to spatial smoothing kernels of 31 *pixels* or larger. It is interesting that a comparison of the total error map for the hardening modulus of the linear model (see Figure 12 (f)) to the total error of the long term hardening modulus of the Voce model, R_0, shows a reasonable match given that the plots in Figure 17 exclude the no smoothing cases.

Now let us consider the identification of the Voce hardening law using the SB virtual fields as shown in Figure 18. Comparison of the error maps for the two materials shows similar trends but total error on the yield parameters is generally higher for the steel case. The range over which the error is low on the R_0 and b parameters is also narrower for steel. It is also interesting that the error maps are similar when comparing the SB virtual fields to the SG virtual field. An overall analysis of Figures 17 and 18 shows that there is a region at a spatial smoothing kernel of 31 *pixels* that seems to return a low total error for all parameters.

Analysis of the total error from the 1D stress-strain curve is shown in Figure 19. Here we see that the SG virtual field returns a low error for all cases that avoid the region of noise induced bias (*i.e.* the cases where no smoothing is used). The region over which the noise induced bias

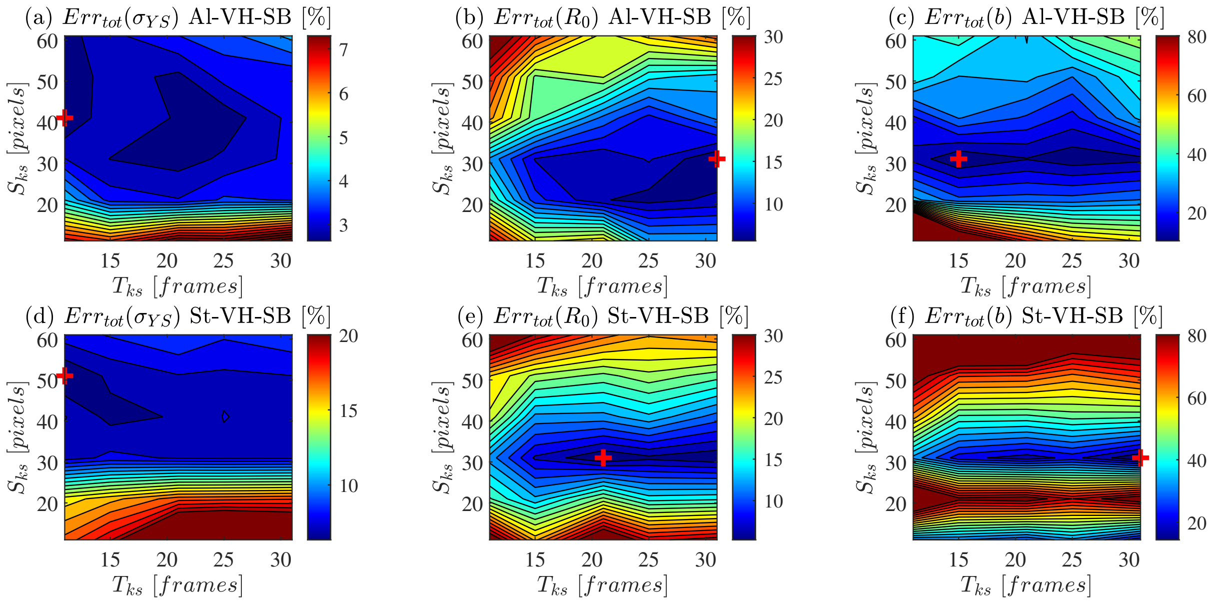

Figure 18: Total error maps for the Voce hardening (VH) law when using the sensitivity-based (SB) virtual fields for the identification. Results on the left show the aluminium (Al) case and results on the right show the steel (St) case.

affects the SB virtual fields seems to be larger, which is consistent with the previously analysed linear model showing that the SB virtual fields tended to favour more spatial smoothing.

An interesting feature of Figure 19 (a) is that the minimum error for the aluminium Voce hardening case when using the SG virtual field occurs with a spatial smoothing kernel of only 11 $pixels$. This corresponds to a point at which the b parameter goes to infinity and the Voce model becomes similar to the linear case. In order to more accurately capture the b parameter the point with minimum error and a spatial smoothing kernel of at least 31 $pixels$ was taken. The difference in total error between these two cases is small.

The optimal smoothing parameters that give the minimum total error on the 1D stress-strain curve for all cases are summarised in Table 5. The stress-strain curves for the optimal cases given in Table 5 are shown in Figure 20. Analysis of this figure shows that the identification of the Voce model is similar to the behaviour of the linear hardening case. This is especially evident when contrasting the two types of virtual fields used, with the SB virtual fields tending to undercut the yield stress and overshoot the long term hardening modulus. Here we also see that the transition region described by the b parameter is only a small part of the response explaining why the identification of the aluminium Voce model with the SG virtual field favouring a solution where the b parameter was not able to be identified.

Overall, the predicted identification errors for the Voce model are fairly low as long as enough smoothing is applied to avoid the region of noise-induced bias (*i.e.* smoothing kernels above $T_{ks} = 11$ $frames$ and $S_{ks} = 21$ $pixels$). These results show that ultra-high speed cameras with low grey level noise should be favoured for the elasto-plasticity identification procedure developed in this work. Fortunately, this is the case for the Shimadzu HPV-X camera modelled here. Once technology improves and pixel array sizes increase on the latest generation of ultra-high speed cameras this requirement could be relaxed somewhat as the increased spatial resolution would allow larger smoothing kernels to be applied without compromising the systematic error.

These results are also encouraging because it should be possible to use more interesting geometry to increase the heterogeneity of the fields without drastically increasing the identification

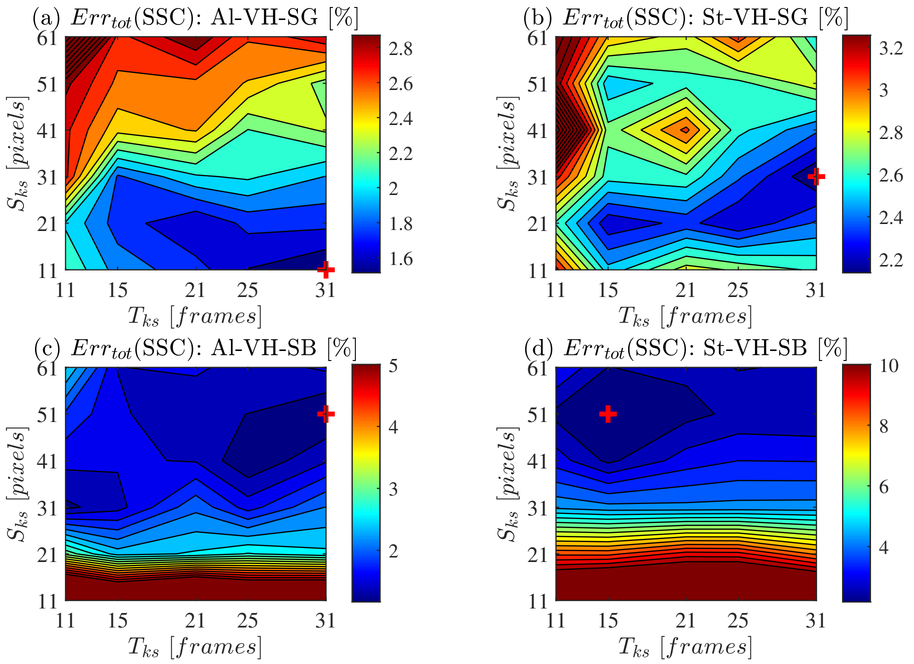

Figure 19: Total error maps on the 1D stress-strain curve for the Voce hardening law when using the stress-gauge (SG) virtual field or the sensitivity-based (SB) virtual fields for the identification. Results on the left show the aluminium (Al) case and results on the right show the steel (St) case.

	Aluminium (Al)		Steel (St)	
	Stress-Gauge (SG)	Sensivity-Based VFs (SB)	Stress-Gauge (SG)	Sensivity-Based VFs (SB)
T_{ks} $[frames]$	15	31	31	15
S_{ks} $[pixels]$	31	51	31	51
Err^{+}_{sys}(SSC) [%]	1.39	0.82	1.73	1.65
Err_{rnd}(SSC) [%]	0.22	0.17	0.20	0.26
Err_{tot}(SSC) [%]	1.83	1.17	2.14	2.18
$\sigma_0(med/ref)$	0.94	0.88	0.98	0.91
$\sigma_0(MAD/ref)$ [%]	1.91	5.28	0.80	3.47
$R_0(med/ref)$	0.99	1.09	0.98	1.12
$R_0(MAD/ref)$ [%]	2.32	2.46	1.06	3.73
$R_{inf}(med/ref)$	1.07	1.16	0.96	1.05
$R_{inf}(MAD/ref)$ [%]	4.00	8.79	1.06	5.08
$b(med/ref)$	1.01	1.20	1.03	1.50
$b(MAD/ref)$ [%]	3.47	9.88	2.52	9.85
$\sigma_{YS}(med/ref)$	0.98	0.98	0.98	0.95
$\sigma_{YS}(MAD/ref)$ [%]	0.22	0.54	0.31	0.89

Table 5: Optimal smoothing parameters for the Voce hardening law and resulting median identified model parameters and median absolute deviations (MAD).

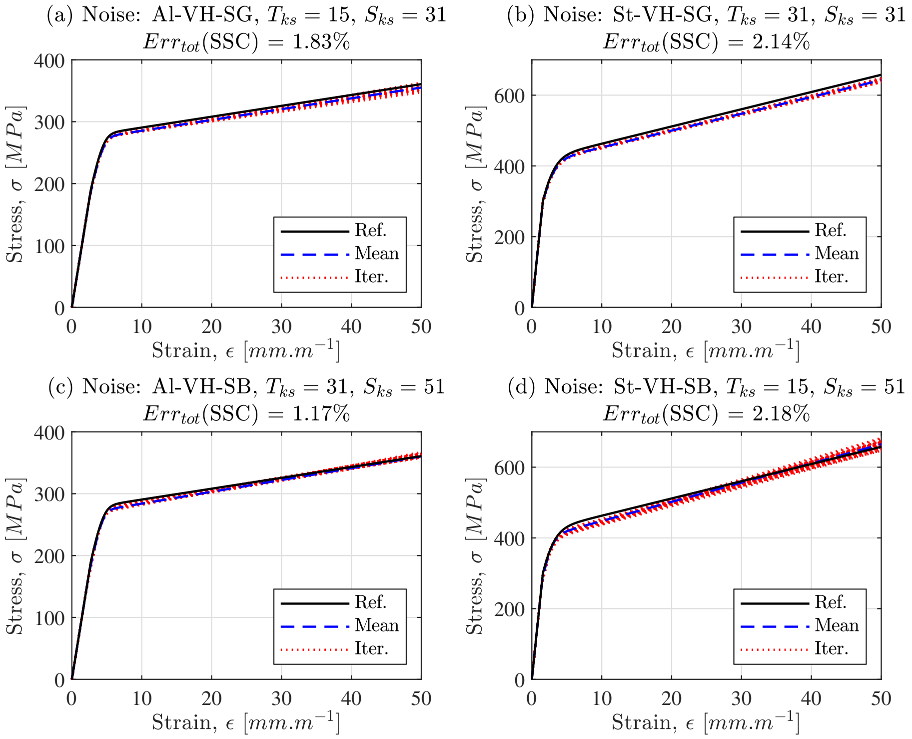

Figure 20: Stress-strain curves for all thirty copies of noise (Iter.) when using the optimal smoothing parameter for the Voce hardening models. The reference curve (Ref.) and average identified curve (Mean) are also given to indicate the overall distribution of the curves.

error, which mainly results from noise-induced bias. When using more complex geometry the presence of sharp gradients at free edges will be an issue. However, the same image deformation analysis tool used in this study can be used to assess different methods of edge reconstruction in a rational manner. This should enable the use of more complex geometry in the future, as in [27].

5 Conclusion

This study has presented the development and validation of the VFM theory required for elasto-plastic material property identification at high strain rates using the IBII test. Following validation of the theory a thorough analysis of measurement errors was performed using synthetic image deformation simulations. The main outcomes of this work can be summarised as follows:

1. An elasto-plastic VFM identification procedure was developed and validated on finite element data for linear and Voce hardening models.

2. For the simple rectangular sample geometry considered here the predicted systematic error for both types of virtual fields for the noise free case is remarkably low (on the order of a few percent or less) given the camera spatial resolution.

3. There is a significant noise-induced bias on the identification. This comes from the interaction between return mapping algorithm and noisy strain data resulting in spurious elastic unloading.

4. As long as a reasonable amount of smoothing is applied it is possible to mitigate the noise-induced bias and the required amount of smoothing can be estimated using a simple comparison between FE and noisy image deformation data.

5. Optimal smoothing parameters were selected for all cases (aluminium/steel, linear/Voce hardening and stress-gauge/sensitivity-based virtual fields) with all cases giving a predicted total error on the 1D stress-strain curve of less than 3%.

6. The sensitivity-based virtual fields generally returned lower total errors than the stress-gauge virtual field and tend to favour higher spatial smoothing kernels. However, the overall difference in error magnitude was small (less than 1%).

It is important to emphasise here that synthetic image deformation simulations are an extremely useful tool for understanding the effects of processing parameters and experimental errors on inverse identification procedures. The key here is that the image deformation simulation is based on a set of known kinematics which encode a set of reference parameters, allowing for direct comparison. If one was blindly processing experimental data it would have been difficult to deduce optimal processing parameters and this could lead to large identification errors. While the noise-induced bias is dominant for the simple geometry considered here this may not be the case when geometrical features such as holes and notches are used to increase the heterogeneity of the kinematic fields. This is an obvious next step for developing the IBII methodology, allowing more complex material behaviour to be identified in a single test. However, the current spatial resolution of ultra-high speed cameras constrains the ability to resolve sharp gradients in the kinematic fields and leads to a large area of data being lost at free edges. Nevertheless, the use of image deformation simulations allows the error associated with camera resolution to be quantified as well as answering the follow up question ‘What camera and test configuration would I need to be able to resolve all parameters of a given material model in a single test?’ This is a very important question that is currently under-researched [48]. A first attempt has been made in [26, 27] to identify rate sensitivity parameters for visco-plasticity using specimens with holes and notches.

Having developed a procedure for elasto-plastic material property identification the next step is to apply the method to experimental data. Therefore, the next paper in this two part series applies the theory and processing methodology developed in this work to validate the approach on experimental data.

Acknowledgements

Prof. Pierron and Dr Dreuilhe acknowledge support from US Air Force / EOARD (grant FA8655-13-1-3041). The authors are grateful to the EOARD program manager, Dr Matt Snyder, for supporting this work. Dr Frances Davis, Dr Lloyd Fletcher and Prof. Fabrice Pierron acknowledge support from EPSRC through grant EP/L026910/1.

This material is based on research sponsored by the Air Force Research Laboratory, under agreement number FA8655-13-1-3041. The U.S. Government is authorized to reproduce and distribute reprints for Governmental purposes notwithstanding any copyright notation thereon. The views and conclusions contained herein are those of the authors and should not be interpreted as necessarily representing the official policies or endorsements, either expressed or implied, of the Air Force Research Laboratory or the U.S. Government.

Data Provision

All data supporting this study are openly available from the University of Southampton repository at: http://dx.doi.org/10.5258/SOTON/xxxxx. The digital dataset contains the following:

1. Python code used to generate the Abaqus FE models for each case: aluminium/steel and linear/Voce hardening
2. Matlab programs for generating synthetic grid images from Abaqus FE data
3. Matlab programs for performing the identification procedure on FE data
4. Matlab programs for running the parametric smoothing sweep in parallel using either the stress-gauge virtual field or the sensitivity-based virtual fields.
5. Synthetic images generated for all cases: aluminium/steel and linear/Voce hardening
6. All error maps not included in the main manuscript.

Appendix

The purpose of this appendix is to provide further explanation for the streaking pattern observed in the stress-gauge error field shown in Figure 16. Here we consider a simple one dimensional sample of length 70 mm discretised into a series of 'pixels' with spacing of 0.2 mm. We then propagate a triangular acceleration front along the sample as shown in Figure 21 (a). The peak acceleration of the triangular wave front has been set to -6×10^6 $m.s^{-2}$. Now, we pollute the acceleration with random noise using a normal distribution with a standard deviation of 3×10^6 $m.s^{-2}$. The noisy wave propagation diagram is shown in Figure 21 (b). Our goal is to calculate the average stress using the stress-gauge equation (equation 4) so the first step is to obtain the surface average of acceleration from the free edge ($x = 0$) to the point of interest. This is shown in Figure 21 (c) for the no noise case and Figure 21 (d) for the noisy case. Figure 21 (d) shows that the points near the free edge are more affected by noise as the surface average is conducted over a limited number of points. Finally, we calculate the stress using the stress-gauge equation by multiplying by the density (taking $\rho = 2700$ $kg.m^{-3}$) and the distance from the free edge. The average stress calculated using the stress-gauge equation if shown in Figure 21 (e) for the no noise case and in Figure 21 (f) for the noisy case.

The error between the no noise (Figure 21 (e)) and noisy case (Figure 21 (f)) can now be calculated as shown in Figure 22. Note that the error has been normalised by the peak compressive stress observed for the no noise case and expressed as a percentage. Here we see that the streaking pattern observed previously (see Figure 16 (c) and (d)) is replicated. This result comes from the surface average of acceleration, which can be biased if there are a cluster of noisy data points which all either over or under shoot the true value. These points are carried forward in the cumulative surface average leading to the streaking pattern observed for the noisy case. Considering the results in Figure 21 (d) where the acceleration surface average has a large random error, it seems counter intuitive that the error on the stress is low near the free edge. However, if we consider the stress-gauge equation we see that all points are weighted by the distance from the free edge. Therefore, the acceleration surface average near the free edge carries minimal weight in the overall stress calculation. This demonstrates that the streaking pattern shown in Figure 16 (c) and (d) is mainly a result of noise.

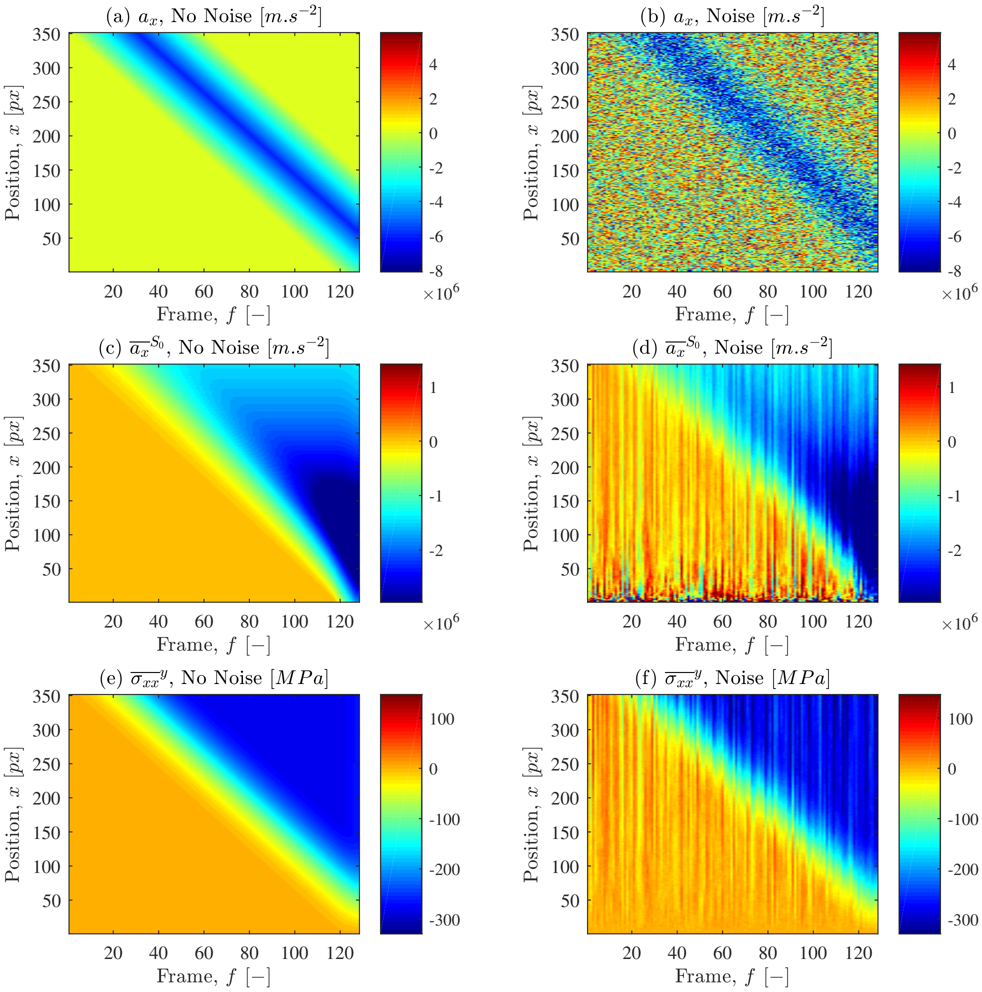

Figure 21: Simple one dimensional wave propagation model used to investigate the noise-induced streaking pattern in the error map given in Figure 16 (c) and (d).

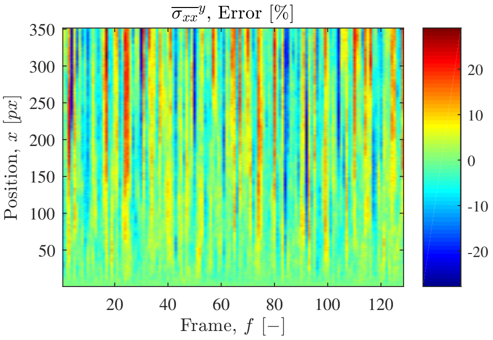

Figure 22: Percentage error between the average stress for the no noise (see Figure 21 (e)) and noisy case (see Figure 21 (f)). Note that the error has been normalised by the peak compressive stress for the no noise case.

References

[1] J. E. Field, S. M. Walley, W. G. Proud, H. T. Goldrein, and C. R. Siviour. Review of experimental techniques for high rate deformation and shock studies. *International Journal of Impact Engineering*, 30(7):725–775, August 2004.

[2] B. A. Gama, S. L. Lopatnikov, and J. W. Gillespie. Hopkinson bar experimental technique: a critical review. *Applied Mechanics Reviews*, 57(4):223–250, October 2004.

[3] M. Rossi, F. Pierron, and P. Forquin. Assessment of the metrological performance of an in situ storage image sensor ultra-high speed camera for full-field deformation measurements. *Measurement Science and Technology*, 25(2):025401, February 2014.

[4] P. L. Reu. High/ultra-high speed imaging as a diagnostic tool. In *Advances in Experimental Mechanics VIII*, volume 70 of *Applied Mechanics and Materials*, pages 69–74. Trans Tech Publications, 2011.

[5] M. A. Sutton, J. J. Orteu, and H. Schreier. *Image correlation for shape, motion and deformation measurements: basic concepts, theory and applications.* Springer Science & Business Media, April 2009.

[6] M. Grédiac, F. Sur, and B. Blaysat. The grid method for in-plane displacement and strain measurement: a review and analysis. *Strain*, 52(3):205–243, June 2016.

[7] V. Tarigopula, O. S. Hopperstad, M. Langseth, A. H. Clausen, and F. Hild. A study of localisation in dual-phase high-strength steels under dynamic loading using digital image correlation and FE analysis. *International Journal of Solids and Structures*, 45(2):601–619, January 2008.

[8] A. Gilat, T. E. Schmidt, and A. L. Walker. Full field strain measurement in compression and tensile split Hopkinson bar experiments. *Experimental Mechanics*, 49(2):291–302, April 2009.

[9] J. Kajberg, K. G. Sundin, L. G. Melin, and P. Ståhle. High strain-rate tensile testing and viscoplastic parameter identification using microscopic high-speed photography. *International Journal of Plasticity*, 20(4):561–575, April 2004.

[10] J. Kajberg and B. Wikman. Viscoplastic parameter estimation by high strain-rate experiments and inverse modelling – Speckle measurements and high-speed photography. *International Journal of Solids and Structures*, 44(1):145–164, January 2007.

[11] J. Peirs, P. Verleysen, W. Van Paepegem, and J. Degrieck. Determining the stress–strain behaviour at large strains from high strain rate tensile and shear experiments. *International Journal of Impact Engineering*, 38(5):406–415, May 2011.

[12] R. Moulart, F. Pierron, S. R. Hallett, and M. R. Wisnom. Full-field strain measurement and identification of composites moduli at high strain rate with the virtual fields method. *Experimental Mechanics*, 51(4):509–536, November 2010.

[13] F. Pierron and P. Forquin. Ultra-high-speed full-field deformation measurements on concrete spalling specimens and stiffness identification with the virtual fields method. *Strain*, 48(5):388–405, October 2012.

[14] B. Lukić, D. Saletti, and P. Forquin. On the processing of spalling experiments. part II: identification of concrete fracture energy in dynamic tension. *Journal of Dynamic Behavior of Materials*, 4(1):56–73, March 2018.

[15] P. Forquin and B. Lukić. On the processing of spalling experiments. Part I: identification of the dynamic tensile strength of concrete. *Journal of Dynamic Behavior of Materials*, 4(1):34–55, March 2018.

[16] F. Pierron, H. Zhu, and C. Siviour. Beyond Hopkinson's bar. *Philosophical Transactions of the Royal Society of London A: Mathematical, Physical and Engineering Sciences*, 372(2023), August 2014.

[17] B. Koohbor, A. Kidane, W.-Y. Lu, and Michael A. Sutton. Investigation of the dynamic stress–strain response of compressible polymeric foam using a non-parametric analysis. *International Journal of Impact Engineering*, 91:170–182, May 2016.

[18] B. Koohbor, A. Kidane, and W.-Y. Lu. Effect of specimen size, compressibility and inertia on the response of rigid polymer foams subjected to high velocity direct impact loading. *International Journal of Impact Engineering*, 98:62–74, December 2016.

[19] S.-H. Yoon, M. Winters, and C. R. Siviour. High strain-rate tensile characterization of EPDM rubber using non-equilibrium loading and the virtual fields method. *Experimental Mechanics*, 56(1):25–35, January 2016.

[20] S.-H. Yoon and C. R. Siviour. Application of the virtual fields method to rubbers under medium strain rate deformation using both acceleration and traction force data. *Journal of Dynamic Behavior of Materials*, 3(1):12–22, March 2017.

[21] S.-H. Yoon and C. R. Siviour. The incremental Virtual Fields Method and prestretching method applied to rubbers under uniaxial medium-strain-rate loading. *Strain*, 53(3):e12225, 2017.

[22] L. Fletcher, J. Van-Blitterswyk, and F. Pierron. A novel image-based inertial impact test (IBII) for the transverse properties of composites at high strain rates. *Journal of Dynamic Behavior of Materials*, 5(1):65–92, March 2019.

[23] J. Van Blitterswyk, L. Fletcher, and F. Pierron. Image-based inertial impact test for composite interlaminar tensile properties. *Journal of Dynamic Behavior of Materials*, 4(4):543–572, December 2018.

[24] L. Fletcher, J. Van-Blitterswyk, and F. Pierron. Combined shear/tension testing of fibre composites at high strain rates using an image-based inertial impact test. In *EPJ Web of Conferences*, volume 183, page 02041, 2018.

[25] L. Fletcher and F. Pierron. An image-based inertial impact (IBII) test for tungsten carbide cermets. *Journal of Dynamic Behavior of Materials*, 4(4):481–504, December 2018.

[26] P. Bouda, B. Langrand, D. Notta-Cuvier, E. Markiewicz, and F. Pierron. A computational approach to design new tests for viscoplasticity characterization at high strain-rates. *Computational Mechanics*, June 2019.

[27] T. Fourest, P. Bouda, L. C. Fletcher, D. Notta-Cuvier, E. Markiewicz, F. Pierron, and B. Langrand. Image-based inertial impact test for characterisation of strain rate dependency of Ti6Al4V titanium alloy. *Experimental Mechanics*, 60(2):235–248, February 2020.

[28] L. Djapic Oosterkamp, A. Ivankovic, and G. Venizelos. High strain rate properties of selected aluminium alloys. *Materials Science and Engineering: A*, 278(1):225–235, February 2000.

[29] W. Moćko, J. A. Rodríguez-Martínez, Z. L. Kowalewski, and A. Rusinek. Compressive viscoplastic response of 6082-T6 and 7075-T6 aluminium alloys under wide range of strain rate at room temperature: experiments and modelling. *Strain*, 48(6):498–509, 2012.

[30] J. Zhou, M. Hayden, and X. Gao. An investigation of the strain rate and temperature effects on the plastic flow stress and ductile failure strain of aluminum alloys 5083-H116, 6082-T6 and a 5183 weld metal. *Proceedings of the Institution of Mechanical Engineers, Part C: Journal of Mechanical Engineering Science*, 227(5):883–895, May 2013.

[31] X. Chen, Y. Peng, S. Peng, S. Yao, C. Chen, and P. Xu. Flow and fracture behavior of aluminum alloy 6082-T6 at different tensile strain rates and triaxialities. *PLOS ONE*, 12(7):e0181983, July 2017.

[32] W.-S. Lee, C.-F. Lin, and T.-J. Liu. Impact and fracture response of sintered 316L stainless steel subjected to high strain rate loading. *Materials Characterization*, 58(4):363–370, April 2007.

[33] W.-S. Lee, C.-F. Lin, T.-H. Chen, and W.-Z. Luo. High temperature deformation and fracture behaviour of 316L stainless steel under high strain rate loading. *Journal of Nuclear Materials*, 420(1):226–234, January 2012.

[34] A. Gilat, V-T. Kuokkala, J. D. Seidt, and J. L. Smith. Full-field measurement of strain and temperature in quasi-static and dynamic tensile tests on stainless steel 316L. *Procedia Engineering*, 207:1994–1999, January 2017.

[35] P. Lava, S. Cooreman, S. Coppieters, M. De Strycker, and D. Debruyne. Assessment of measuring errors in DIC using deformation fields generated by plastic FEA. *Optics and Lasers in Engineering*, 47(7–8):747–753, July 2009.

[36] P. Lava, S. Cooreman, and D. Debruyne. Study of systematic errors in strain fields obtained via DIC using heterogeneous deformation generated by plastic FEA. *Optics and Lasers in Engineering*, 48(4):457–468, April 2010.

[37] M. Rossi and F. Pierron. On the use of simulated experiments in designing tests for material characterization from full-field measurements. *International Journal of Solids and Structures*, 49(3):420–435, February 2012.

[38] B. Lukić, D. Saletti, and P. Forquin. Use of simulated experiments for material characterization of brittle materials subjected to high strain rate dynamic tension. *Phil. Trans. R. Soc. A*, 375(2085):20160168, January 2017.

[39] A. Marek, F. M. Davis, and F. Pierron. Sensitivity-based virtual fields for the non-linear virtual fields method. *Computational Mechanics*, 60(3):409–431, September 2017.

[40] N. Nsiampa, J. P. Ponthot, and L. Noels. Comparative study of numerical explicit schemes for impact problems. *International Journal of Impact Engineering*, 35(12):1688–1694, December 2008.

[41] L. Maheo, G. Rio, and V. Grolleau. On the use of some numerical damping methods of spurious oscillations in the case of elastic wave propagation. *Mechanics Research Communications*, 38(2):81–88, March 2011.

[42] G. Noh and K.-J. Bathe. An explicit time integration scheme for the analysis of wave propagations. *Computers & Structures*, 129:178–193, December 2013.

[43] E. A. de Souza Neto, D. Peric, and D. R. J. Owen. *Computational methods for plasticity: theory and applications*. John Wiley & Sons, September 2011.

[44] A. Marek, F. M. Davis, M. Rossi, and F. Pierron. Extension of the sensitivity-based virtual fields to large deformation anisotropic plasticity. *International Journal of Material Forming*, 12(3):457–476, May 2019.

[45] M. Rossi, P. Lava, F. Pierron, D. Debruyne, and M. Sasso. Effect of DIC spatial resolution, noise and interpolation error on identification results with the VFM. *Strain*, 51(3):206–222, June 2015.

[46] L. Fletcher, J. Van Blitterswyk, and F. Pierron. A manual for conducting image-based inertial impact (IBII) tests, August 2019. http://dx.doi.org/10.5258/SOTON/P0015.

[47] M. Grédiac, B. Blaysat, and F. Sur. A critical comparison of some metrological parameters characterizing local digital image correlation and grid method. *Experimental Mechanics*, 57(6):871–903, July 2017.

[48] F. Pierron and M. Grédiac. Towards material testing 2.0: a review of test design for identification of constitutive parameters from full-field measurements. *Strain*, 2020. Submitted.